FACULDADE DE ENGENHARIA DA UNIVERSIDADE DO PORTO


FEUP

# Computational vision applied to the segmentation and morphometric characterization of the sciatic nerve in microscopic images

**Diogo Machado Carneiro Dias**

Master in Informatics and Computing Engineering

Supervisor: Jaime dos Santos Cardoso (PhD)

Second Supervisor: Hélder Filipe Pinto de Oliveira (MSc)

July 3, 2011

# Computational vision applied to the segmentation and morphometric characterization of the sciatic nerve in microscopic images

**Diogo Machado Carneiro Dias**

Master in Informatics and Computing Engineering

Approved in oral examination by the committee:

Chair: Luís Filipe Pinto de Almeida Teixeira (PhD)

External Examiner: Hugo Pedro Martins Carriço Proença (PhD)

Supervisor: Jaime dos Santos Cardoso (PhD)

---

$13^{rd}$ July, 2010

# Abstract

In everyday life, many processes are considered repetitive. Some of them are extremely time consuming and most of them are tedious. There is at least one thing in common for most of those precesses, if not all: the attempt to automate them. The automation of these processes not only helps making the job more satisfying, by allowing a person to skip the tedious and repetitive tasks, but also frees him to do other, more productive, assignments.

Image analysis is one of such cases. Traditionally, the image analysis was done resorting to manual tools, or simply regarded information gatherable by visual analysis. Due to its importance in many areas, automated image processing has been object of study for long. Medicine and biology are areas that can substantially benefit from automatic image processing. Researchers frequently have to measure structures, count or track them, sometimes in more than just one image. Also, an image might have just a few structures, and be easy to deal with manually, or it might have a few thousands. Automatic image processing can not only help with the repetitive tasks, but also deal with huge amount of data that would be humanly impossible due to time restrictions.

This work aimed to develop a fully automated technique allowing for the segmentation and feature extraction of the axons in a sciatic nerve cut image, obtained with a light microscope. To do so, a segmentation method based on *a priori* knowledge was proposed and implemented, as well as its comparison with segmentation algorithms present on the literature. This new method finds the threshold value that maximizes the number of objects captured that have a single hole. The improvement of the algorithms with postprocessing techniques is also necessary and an objective of this work. After the segmentation step, some structures are merged and there are invalid axons incorrectly considered. It is important to separate the merged axons, as well as to remove the false-positives. Finally, this project aimed to develop a method for feature extraction and characteristics measurement, counting the number of axons in the image and measuring them.

The algorithm suggested in this work managed to segment 88.2% of the pixels correctly. It was only bested by Khashman and Sekeroglu's [KS07] method, henceforward named as Luminance Thresholding, managed to correctly segment 88.5% of the pixels.

Khashman and Sekeroglu's method also performed the best when analysing the whole process of segmentation and characteristics measurement. It measured an average of 2344 structures per image, which represents an 837.5% increase when compared to the 250 that are currently taken into account by the manual processes regarded in this study. The Mean Squared Error of the global measurement was 0.014, which represents 2.1% of the average G-Ratio value in the images used.

# Resumo

No dia a dia, existem muitos processos considerados repetitivos. Alguns são extramamente demorados e a maioria é considerada entediante. Existe algo comum a quase todos os processos, senão todos: a tentativa de os automatizar. Isto não só torna o trabalho mais satisfatório, ao permitir que o indivíduo evite tarefas aborrecidas e repetitivas, como também o liberta para realizar outras tarefas, normalmente mais produtivas.

O análise automática de imagem é um destes casos. Tradicionalmente, a análise das imagens recorria a ferramentas manuais, ou era simplesmente limitada a recolha de informação obtida visualmente. Devido à sua importância nas mais diversas áreas, o processamento de imagem automatizado tem sido alvo de estudo há muitos anos. A medicina e a biologia são áreas que podem benificiar substancialmente do processamento de imagem automatizado. Os investigadores têm uma necessidade frequente de medir estruturas, contar ou rastreá-las, por vezes recorrendo a mais do que uma imagem. Além disso, cada imagem pode ter apenas algumas estruturas, e ser facilmente analisada manualmente, mas também pode ter milhares de estruturas. O processamento de imagem automatizado não só pode ajudar na realização de tarefas repetitivas como também pode trabalhar com enormes quantidades de informação que seria impossível ser tratada humanamente devido a restrições, normalmente, temporais.

Este trabalho teve como objectivo o desenvolvimento de um método totalmente automatizado para a segmentação e medição de características dos axónios em imagens do nervo ciático, obtidas com um microscópio óptico. Para isso, um algoritmo de segmentação baseado em conhecimento *a priori* sobre o problema foi pruposto e implementado, assim como a comparação deste com outros algoritmos de segmentação presentes na literatura. Este novo método consiste em procurar o *threshold* que maximiza o número de objectos obtidos que têm um e apenas um buraco. O melhoramento dos resultados obtidos através de técnicas de pós-processamento é também necessário e parte integrante deste trabalho. Depois do passo de segmentação, algumas estruturas estão unidas e existem axónios que são erradamente considerados. É importante separar os que estão juntos, assim como remover os axónios inválidos. Finalmente, o projecto teve como objectivo o desenvolvimento de um método para extracção e medição de características dos axónios, a partir de imagens segmentadas. É necessário fazer a contagem do número das estruturas assim como medir as dimensões de cada uma delas.

O algoritmo sugerido neste trabalho conseguiu segmentar correctamente 88.2% dos píxeis das images, em média. O único algoritmo que conseguiu um resultado melhor foi o proposto por Khashman and Sekeroglu [KS07], designado neste trabalho como *Luminance Thresholding*, com uma média de 88.5%.

O método proposto por Khashman and Sekeroglu's conseguiu também o melhor resultado na avaliação global do processo. Este algoritmo detectou uma média de 2344

estruturas por imagem, o que representa um aumento de 837.5% comparativamente às 250 estruturas medidas no processo manual considerado no estudo. O Erro Quadrático Médio das medições globais foi de 0.014, o que representa aproximadamente 2.1% da média dos G-Ratio das imagens consideradas.

# Acknowledgements

To Professor Jaime dos Santos Cardoso, for his supervision, useful input and guidance throughout this project.

To Filipe Tiago Alves de Magalhães for all his support and input during this project.

To Hélder Filipe Pinto de Oliveira for his friendship, close supervision and huge time spent.

To INESC Porto, the Visual Computing and Machine Intelligence (VCMI) in particular, for the great work environment, the support and the opportunity to learn so much.

To IBMC, in particular to Dr. Pedro Brites for all the support and availability.

To my parents, for the wonderful education and excellent opportunities they gave me from the very first day of my life. (*Aos meus pais, pela maravilhosa educação e excelentes oportunidades que me proporcionaram, desde o meu primeiro dia de vida.*)

To Raquel Vilela, for the close friend and companionship, huge support and true love, and for standing by my side and making these the greatest years of my life.

To my very closest friends, Paulo Silva, Luís Rocha, Tiago Marques, Carina Sousa, Micael Pinho, Inês Morgado and, obviously, João Soares, for all the great and unforgettable moments throughout these years, and for helping me keep my sanity whenever I was close to losing it.

Diogo Machado Carneiro Dias

*"Be the change you want to see in the world."*

Mohandas Karamchand Gandhi

# Contents

# List of Figures

LIST OF FIGURES

# List of Tables

# Abbreviations

| | |
|---|---|
| IBMC | *Instituto de Biologia Molecular e Celular* (Institute for Molecular and Cell Biology) |
| INESC Porto | *Instituto de Engenharia de Sistemas e Computadores do Porto* (Institute for Systems and Computer Engineering of Porto) |
| CNS | Central Nervous System |
| PNS | Peripheral Nervous System |
| BLIST | Binarization Based in Line Spacing and Thickness |
| MSE | Mean Squared Error |

# Chapter 1

# Introduction

## 1.1 Contextualization

This project was developed on *Instituto de Engenharia de Sistemas e Computadores do Porto* (INESC Porto) within the Visual Computing and Machine Intelligence Group (VCMI), under the supervision of Professor Jaime dos Santos Cardoso and Eng. Hélder Filipe Pinto de Oliveira. INESC Porto is a private non-profit association, recognized as Public Interest Institution, created with the objective of being an interface between the academic world and the industry. INESC Porto divides its activities between scientific research and technological development as well as consulting and advanced training. It is also related to *Biostar*, a group of students from the Engineering Faculty of University of Porto with interest in Bio-engineering related areas.

*Instituto de Biologia Molecular e Celular* (IBMC), is a Portuguese institute that does research in the area of the multidisciplinary Life Sciences, aiming to find innovative answers to biologically relevant medical questions. Much of the research done on IBMC requires manual manipulation and processing of microscopic images wasting highly qualified resources that could, otherwise, be assigned to other tasks. For that reason, IMBC and INESC Porto have collaborated in order to achieve the development of methods to automate the image analysis processes.

## 1.2 Motivation

When doing medicine and biologic related research, much information is not visible unless resorting to specific technologies. Microscopy is of fundamental importance to the researchers, as it provides them indispensable information regarding health problems. Information gathered from these images may allow a researcher to detect or identify

health problems or even track their causes. Traditionally, the specialists gather visual hints present in the images or, in case it is needed, measure the characteristics by manual means. These processes are very repetitive, and the number of structures of interest might make it difficult for the researcher to keep track of his actions. Therefore, it is often described as a tedious and time consuming process, and also very susceptible to human errors [ZPW+10, dSJF07]. In order to help the researcher perform their tasks, automatic and semi-automatic methods have been suggested through literature. These methods aid the researchers, allowing them to skip some of the most dull and error prone parts of the process, by extracting and classifying information gathered from microscopic images.

The IBMC Nerve Regeneration group studies the mechanisms related to the process of myelination and regeneration of the nervous system. Amongst the techniques used for this research is the analysis of optical and electron microscopic images of transverse sections of wild type mice nerves. Studying the nerve morphometry, using these images, is of critical importance to IMBC, since it is one of the techniques most used in the research process. Each image contains hundreds or thousands of axons and, therefore, it is an arduous task to count them individually and measure each of them. For that reason, some semi-automated processes have been proposed to help with this task. These processes are based on a manual selection of the threshold and automatic segmentation using the chosen threshold value. The results are, though extremely influenced by the subjectively chosen parameters, which is why IMBC has opted by a manual, albeit software aided, approach.

In order to accelerate the process, only a small percentage of the image is analysed by the specialist, and the values are inferred for the rest of the nerve. This might introduce a significant source of error that, added to the ones caused by manual readings, may lead to incorrect results [dSJF07]. Also, some measurements are done automatically, but the segmentation of each structure is done manually, and the output is related to the measurements of each structure, meaning the results must be introduced somewhere else manually to obtain the global results. Despite the software aid, the process is still arduous and very time consuming.

## 1.3 Objectives

This project aimed to propose a fully automated method that allows to separate the structures in the sciatic nerve images obtained using light microscopy, and to count and measure them, extracting characteristics useful for the researchers, with little effort and time spend.

There are two very distinct problems to be solved: The segmentation and the feature extraction.

To achieve a good segmentation method for this problem, a research on image processing techniques and comparison between them is of major importance. The evaluation

of these techniques will allow for future improvements on this area of research. Also, the introduction of a new method is necessary if the existing ones fail to solve the problem.

A method for extracting the features of the image that are meaningful to the researchers is also indispensable. The results of this step greatly depend on a valid segmentation, so the largest focus of this research was the segmentation process.

## 1.4 Main Contributions

The automatic processes for light microscope images of the sciatic nerve are still very unexplored in literature, hence why this work introduces a few novel contributions.

The methodologies for segmenting and measuring the axons in the sciatic nerve present in the literature focus on electron microscopy images only, thus this novel process may be an important step towards the creation of useful tools for the researchers, since it is fully automated and produces good results. This new methodology is, therefore, the main contribution of this research work.

The segmentation algorithm introduced in this project is also a strong contribution for the literature, since it can be used not only in sciatic nerve images, but also in similar contexts. Also, the comparison between several literature algorithms regarding this specific problem may prove useful for later researches. This comparison was done using a ground truth, partial images manually segmented, which can be useful for future study regarding the sciatic nerve segmentation on light microscopy images.

## 1.5 Document Structure

This document describes the work done during the project and the achieved results. It also contains a review on the state-of-the-art segmentation algorithms regarding their application on this specific problem. The document is divided into seven chapters, the introduction being the first one.

Chapter 2 provides a description of the problem, divided in two sections. Firstly, the biological background related with the problem is described. Then a detailed description of the problem is provided, as well as a study on the automated or semi-automated processes for this problem, present in literature.

The next three chapters describe the automated process created during this project. Each chapter will focus on one of the three steps of the mentioned process. Chapter 3 presents the algorithms used for the segmentation of the structures in the image. Chapter 4 describes an attempt to improve the initial segmentation, by removing objects that were over detected and split the structures that are merged after the initial segmentation phase. Chapter 5 presents the algorithm to extract features from the structures obtained in the previous steps.

Chapter 6 describes the global results, obtained using the three steps of the process.

Finally, Chapter 7 contains the conclusions and future work to be done regarding this specific problem.

# Chapter 2

# Sciatic Nerve Morphometry

## 2.1 Biological Background

Myelin is an electrical insulating material usually found forming a layer around an axon and is referred to as the myelin sheath. This layer is responsible for increased speed of electrical impulses traveling through the axon and helps prevent these impulses from escaping the axon, assuring they reach their destination. As such, the myelin sheath is essential for the development of the nervous system.

On peripheral nerves, Schwann cells are responsible for the myelination process. These cells are distributed along the side of the nerve, and they supply the needed myelin to form the layer. When a peripheral nerve is damaged, Schwann cells generate a myelin layer through the free spaces of the muscles, creating a path for the axon to grow unharmed. The axon will regenerate through this path, which is not necessarily the same as it was before the damage. In fact, it is common for the axon not to find the correct muscle fiber, and for the damaged peripheral nerves to die without regeneration. This inability to provide perfect regeneration usually results in loss of some motor or cognitive functions. The axons of the Central Nervous System (CNS), unlike the ones of the Peripheral Nervous System (PNS), do not regenerate. Since they are enclosed in bone, they are more protected and are less likely to be damaged. On the other hand, should they be damaged, the results are more severe as the nervous tissue cannot be repaired.

A relatively common disease related to the myelin sheath is demyelination. It is the process of loss of myelin sheath surrounding the axons and may be a symptom of neuropathologies. This lack of myelin sheath can severely compromise the ability of the axon to guide the electrical impulse, as it might travel with reduced speed or even leave the axon. As such, demyelination may affect cognitive and motor functions in a way that might range from a slight inability to the total loss of capabilities.

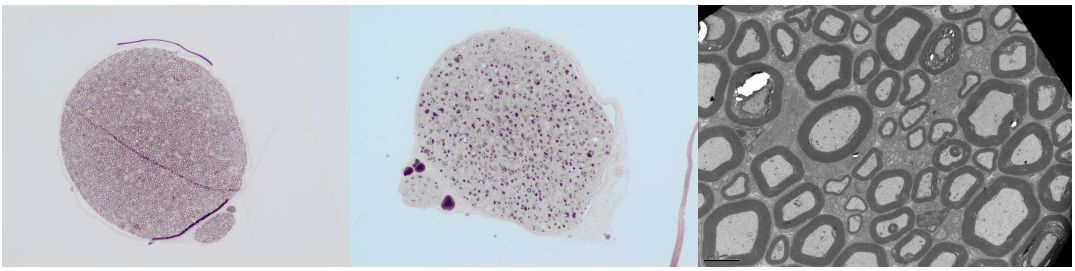

Figure 2.1: (a) Light microscope image of a normal rat nerve captured with ten times amplification; (b) Light microscope image of a crushed rat nerve captured with ten times amplification; (c) Electron microscope image of a normal rat nerve captured with three thousand times amplification.

The study of the myelination process is of fundamental importance to the research for the causes and even the cure of these neuropathies [ZPW+10, dSJF07]. To do so, IBMC researchers use wild type lab rats to investigate the myelin process. Some rats have their sciatic nerve removed while they are totally healthy, while others have it removed after a crush, inducing a nerve lesion. A few transverse sections are then taken from each gathered sciatic nerve, and analysed with both a light and an electron microscope, as shown in Figure 2.1.

The analysis of these images usually focuses on variables such as myelinated axon diameter, perimeter and number, myelin sheath thickness[RCD+00] and, one of the most used, G-Ratio. The latest is widely used due to it being considered highly reliable for axonal myelination assessment, and is defined as the ratio of the inner axonal diameter to the total outer diameter[CH09].

The value of G-Ratio is different for each axon and two apparently similar axons may have myelin layers of different thickness surrounding them. Despite this, the thickness of the myelin sheath and the axon diameter are highly correlated [ZPW+10], the large axons having the thickest layers, and the smaller ones having the slimmest myelin sheaths. The G-Ratio of a nerve is the average value for all the axons measured. According to Chomiak and Hu [CH09], the G-Ratio for fibers of the CNS is usually around 0.77, while the value for a nerve of the PNS is usually not far from 0.60. The sciatic nerve, which belongs to the PNS, has a G-Ratio value ranging from 0.55 to 0.68. These are optimal values of G-Ratio, meaning that different values measured may represent a symptom of some neuropathy.

## 2.2 Problem Description

Each image obtained with a light microscope, as shown in Figure 2.2, contains hundreds or thousands of axons. Figure 2.3 shows a few axons. The darker layers are the myelin sheaths surrounding an axon, which has a colour similar to the background. To count the number of structures, to measure the G-Ratio, perimeter and other important variables of

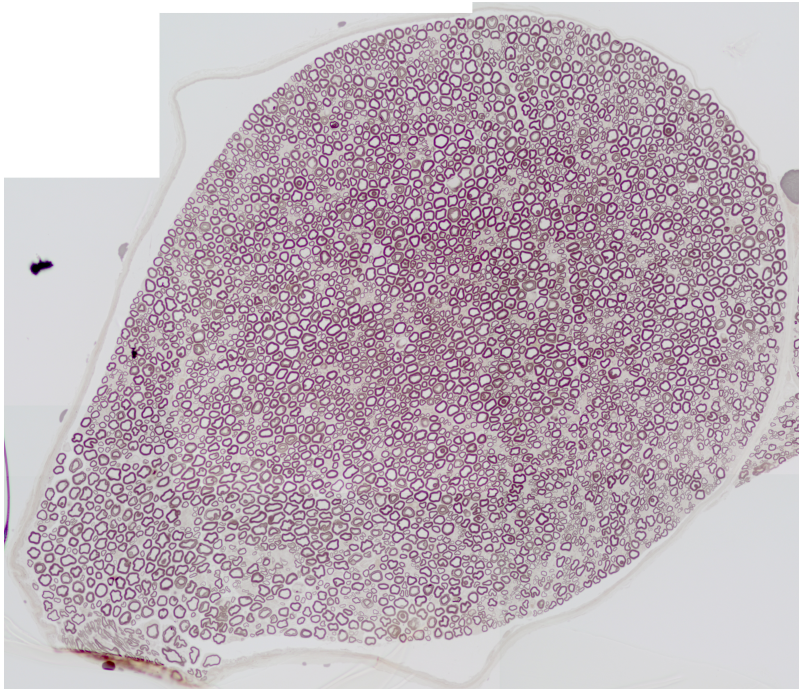

Figure 2.2: Image comprised of several smaller ones manually put together, obtained with a light microscope at forty times amplification.

each of them would be tedious, subject to many sources of errors, difficult to perform correctly and, most of all, extremely time consuming [dSJF07]. Taking into account that more than one image must be analysed each time, and that this task is done by highly qualified resources, a method to improve speed is required. IMBC researchers select a sample of about 2.5% of all structures, count them and measure their G-Ratio. This sampling scheme, though increasing speed when comparing to how long it would take to measure all the structures, is still time consuming. It takes about twenty minutes to analyse each sample. Also, sample schemes may introduce one more source of error [dSJF07], and the process is still tedious and subject to personal interpretation.

Automatic applications may be the solution for this problem, as the process would no longer be tedious, subject to personal interpretation, and highly qualified resources could be assigned to other tasks. Also, no sampling schemes would be required, as automatic methods can deal with huge amounts of data which means more accurate results.

The methods for automatic analysis of microscopic images can be separated into two distinct problems: segmentation and morphometry.

The segmentation is usually the first step in image processing applications, and it is one of the major problems regarding image analysis. It consists of separating the image into its components, based on their similar or different features, such as colour, texture, intensity, shape, usually resorting to *a priori* knowledge. Biomedical segmentation aims to define the regions that correspond to biological entities, and it is typically done by

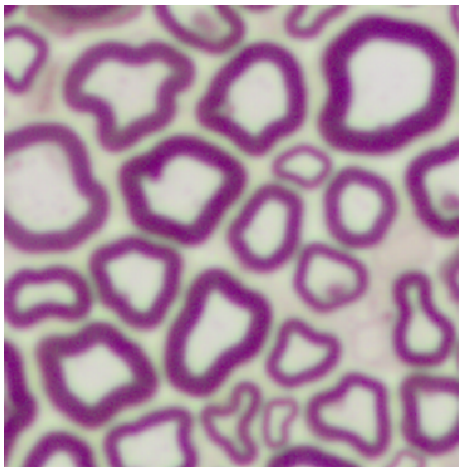

Figure 2.3: Sample of axons as seen through a light microscope.

delineating the structure boundaries, and assigning each pixel of the image to one of the classes (for example, structure and background). Correct segmentation results are often required for most automated computer vision problems, and the performance of the methods is usually judged by comparing them to manual segmentation. There is no global solution to the segmentation of microscopic image. Instead, each solution depends on the application domain, more than on the images themselves. Even though the *a priori* knowledge introduced in the methods can accomplish better results and performances, fully automatic segmentation is sought, but usually not achieved [VH98].

There is a wide panoply of segmentation methods suggested in the literature, with different objectives, implementations and results. Although these methods differ a lot, they have something in common. Besides from simple image processing techniques, such as thresholding or basic edge detection, they usually follow one of two approaches to segmentation: region based or edge based [VM09]. Region based techniques aim to group or separate the image regions according to their common or different properties, respectively. Edge based methods find the pixels in the images that are more likely to be considered structure boundaries, and then link them, thus segmenting the image.

Morphometry is the process of quantitative measurement and analysis of biological structures characteristics, visible either at the microscopic or macroscopic level of detail [VH98]. The information may then be assembled and presented to the user in a more understandable way, like statistics or charts. It is possible that different specialists gather different characteristics from the same images, if they are assigned to different tasks. The morphometry process, just like the segmentation, is application specific. The analysis does not depend on just the image characteristics. In fact, it depends particularly on the goal of the application.

Due to the complex nature of microscopic images, it is hard to develop a method that performs well, being time efficient while providing effective results at the same time,

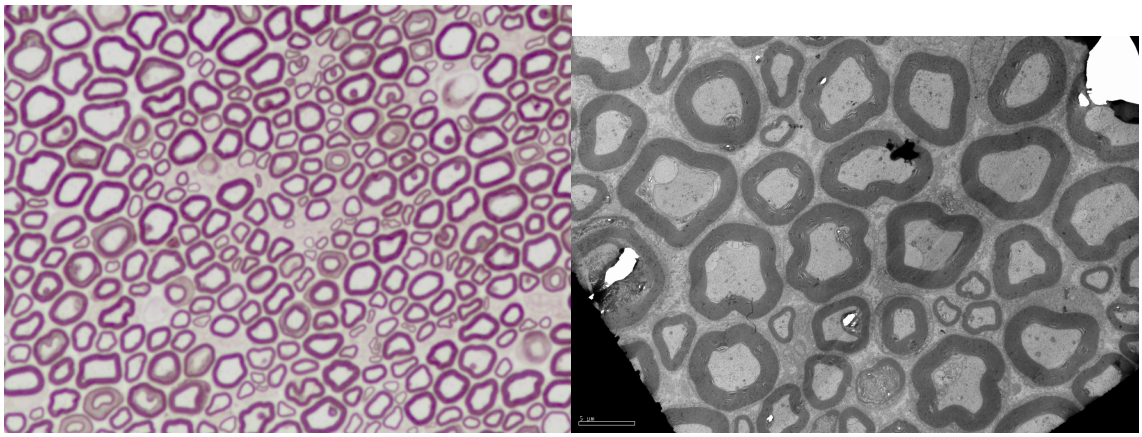

Figure 2.4: (a) Small sample of an image captured with a light microscope with an amplification of forty times; (b) Image captured with an electron microscope with an amplification of three thousand times;

with any type of images in a certain application domain [NAP00]. It is even harder, if not impossible, to develop a method able to deal with all the existing biology or medical segmentation and morphometry problems. That is why most generic biomedical image segmentation applications are based on a collection of methods rather than a single, and more robust, approach [VH98].

### 2.2.1 Segmentation

The segmentation is of fundamental importance to the application. A clear detection and separation of the axons, their respective myelin sheaths and the background are required, as they will have an extreme influence on the posterior measurements.

There are two distinct segmentation problems for which a solution is sought. The electron and light microscope produce different images and the solutions for those problems may differ slightly.

Figure 2.2 is a composition of several light microscopic images. Obtaining images with an amplification of forty times, prevent the researcher from capturing the whole nerve. Therefore, each of its sections must be captured separately and the images are joined together.

As shown in Figure 2.4 the two problems are visually different. The images captured with an electron microscope have better resolution and the boundaries are more clear. On the other hand, the amplification is so high that very few structures are captured at once. For that reason, IMBC researchers also work with light microscope images. Although they lack detail, it is possible to obtain an image of the whole nerve. Due to the lack of resolution and to the huge amount of structures, as shown in Figure 2.2, light microscope images can hardly be precisely segmented, since there is not a clear separation between the axon and the myelin sheath, and between the myelin sheath and the background. Also

a much larger amount of structures need to be segmented in a time effective way. The time may not be of fundamental importance for this problem, but it still is not ignorable.

For these reasons, the segmentation for each of these problems requires separate treatment, although it is expected that the solutions may have some similarities. As stated in Chapter 2.2, segmentation methods commonly use *a priori* knowledge to improve results and time performance and these characteristics are common to both problems.

Regarding the sciatic nerve segmentation problem, some *a priori* knowledge that might be considered useful is presented:

- The axons and the background have approximately the same colour and intensity;
- The axons are surrounded by a layer, clearly distinct from the axon and the background;
- The axons have an imperfect oval shape, with entrances and protuberances;
- Two axons never overlap, although their respective myelin sheaths might not be clearly separated;
- Larger axons have thicker myelin sheaths, while smaller axons have slimmer myelin sheaths. The smaller axons may be hard to detect and segment, but they are important as they are in significant number and their slim myelin sheaths may present a change to the statistics;
- There are some artefacts, like dead axons, in the images. It is possible to ignore these artefacts if there are enough axons to analyse, since they will not change the statistical values;

### 2.2.2 Morphometry

After acquiring a clear separation of the structures, it is necessary to measure the important characteristics. Unlike the segmentation problem, the morphometry is quite similar for both electron and light microscope images.

It is necessary to count the total number of axons, measure their perimeter and diameter and calculate the average value of G-Ratio.

With the segmentation step done, simple morphometry algorithms are enough to measure the characteristics on both types of images, but the amplification of each image must be taken into account. Also, it is expected that, due to the lack of detail of the light microscope images, the values measured on electron microscope images are more accurate.

### 2.2.3 Technical Review

As stated before, multiple domain applications are usually a collection of various methods rather than a single one. Methods with multiple applications are also possible, but their domain is restricted and the results are usually less accurate than a method developed specifically for a problem.

An example of an automated biological image analysis program is CellProfiler™ [LSC07]. This free and open source software allows the user to perform multiple operations like counting colonies, tumour counting in mice or analysing tissue topology. No options could be found to analyse nerve images as required, but the fact that it is free and open source allows for future tool development in this area of study. An example operation of CellProfiler™is shown on Figure 2.5, where cell contours and nuclei are automatically detected.

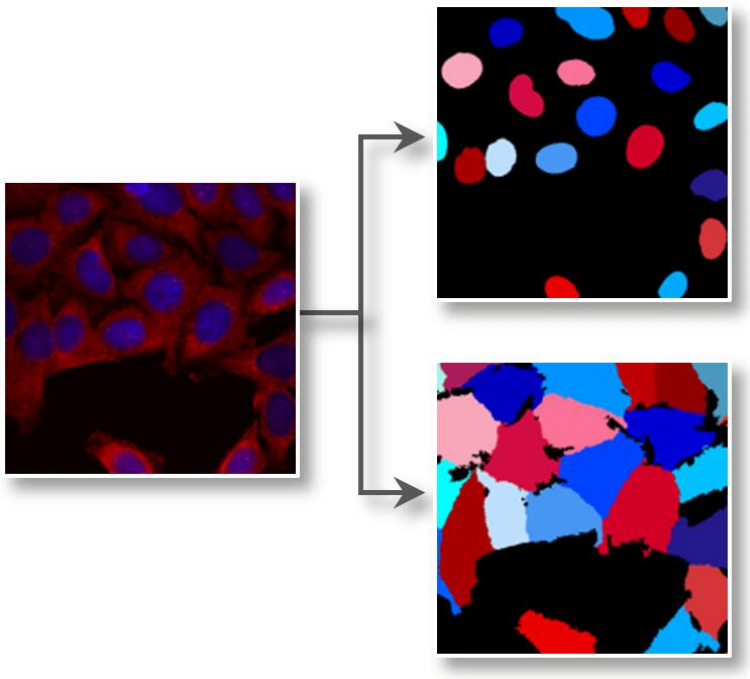

Figure 2.5: CellProfiler™ detecting nuclei and cell contours. Image from http://cellprofiler.org/.

ImageJ[1] is another image processing program, developed in Java. It allows for the development of custom plugins to perform specific operations. Figure 2.6 shows a segmentation done using ImageJ.

[1] http://rsbweb.nih.gov/ij/

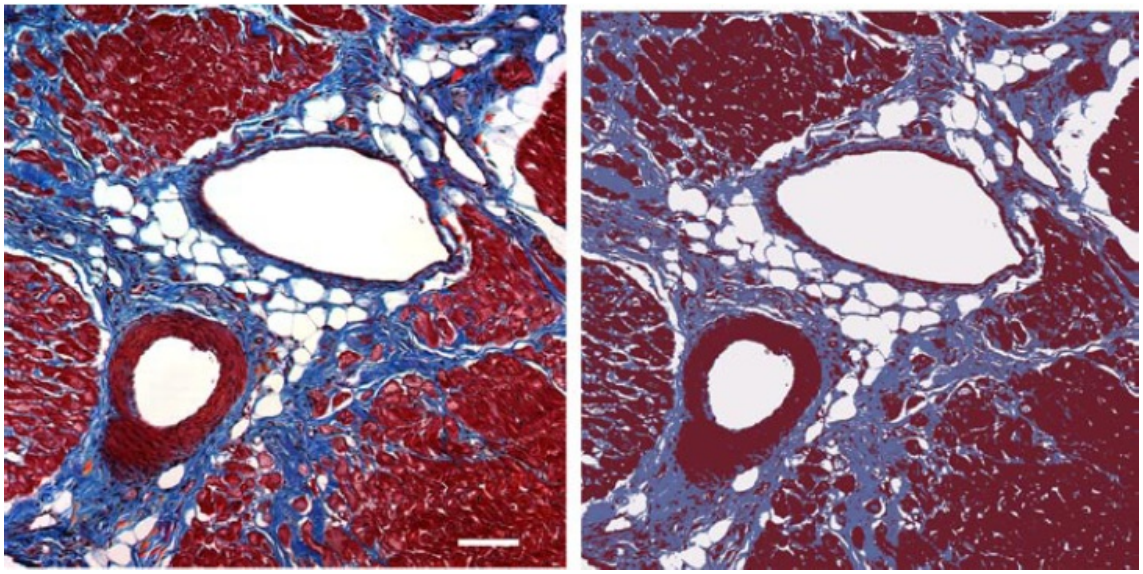

Figure 2.6: Masson's trichrome-stained heart section. On the left is the original picture, and on the right the image segmented into three classes: white background, blue collagen and magenta noncollagen regions. Image from [Col07].

Media Cybernetics[2] developed Image-Pro®, a software with tools to help segment and measure images. This is a powerful tool, and the results can be quite accurate, depending on the user's skill. This application allows computer-aided processes, but not for fully automated methods. Figure 2.7 shows an example of utilization.

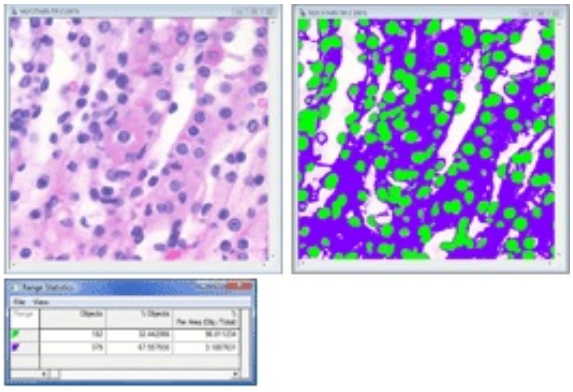

Figure 2.7: Image-Pro®showing the measurements of the thresholded components. Image from http://www.mediacy.com.

There are algorithms used in literature to solve the nerve segmentation problem. A brief description of some of them follows.

[2]http://www.mediacy.com/index.aspx?page=IPP

### 2.2.4 Threshold

Silva *et al.*[dSJF07] proposed an algorithm that performs automatic contrast enhancement and threshold adjustment. The software allows the operator to manually select and separate the fibers that are too close together. The segmentation is done by taking into account pixels colour and brightness.

This method has a few drawbacks, though. First of all, the smaller myelinated axons are ignored by this process, which induces errors in the G-Ratio values. The separation of close cells requires the user to manually separate them, so the process is not totally automated. Finally, this algorithm was developed for electron microscope images only.

### 2.2.5 Region Growing

Zhao *et al.*[ZPW+10] suggested a region growing algorithm binarize the image, and used the maximum gradient magnitude to automatically separate connected myelin sheaths . A binary image obtained with the region growing algorithm is presented in Figure 2.8.

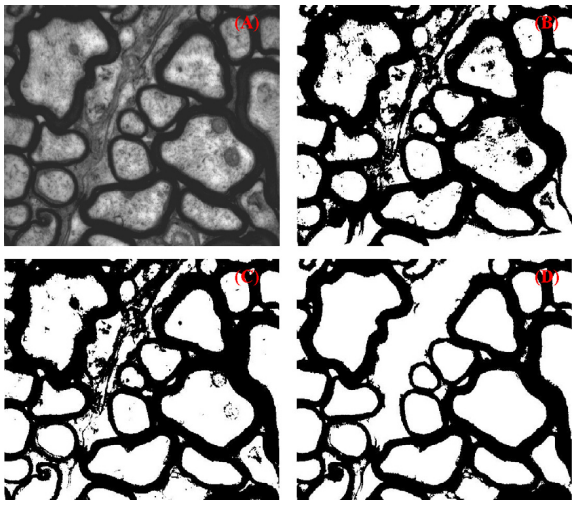


Figure 2.8: (A) Electron microscope image of transverse sections of the optic nerve. (B) Results of a local histogram (50x50) analysis. (C) Results of a local histogram (200x200) analysis. (D) Results of the region growing algorithm. Image from [ZPW+10].

The G-Ratio obtained for rats without neuropathologies using this method was 0.78, which is close to the theoretical value of 0.81 presented by Chomiak *et al.*[CH09] for the optic nerve. The main drawback of this approach is that it was also developed for electron microscope images only.

### 2.2.6 Connected Morphological Operators

Romero *et al.*[RCD+00] suggested a method that binarizes the image using a local threshold. The image is then analysed and a zonal graph is constructed, which is the target of

morphological operations. These operations are used to select the areas of interest, and resort to *a priori* knowledge. The results of this algorithm are good for most fibers, although there are some evident flaws, as can be seen in Figure 2.9. However, this algorithm was also developed for electron microscope images.

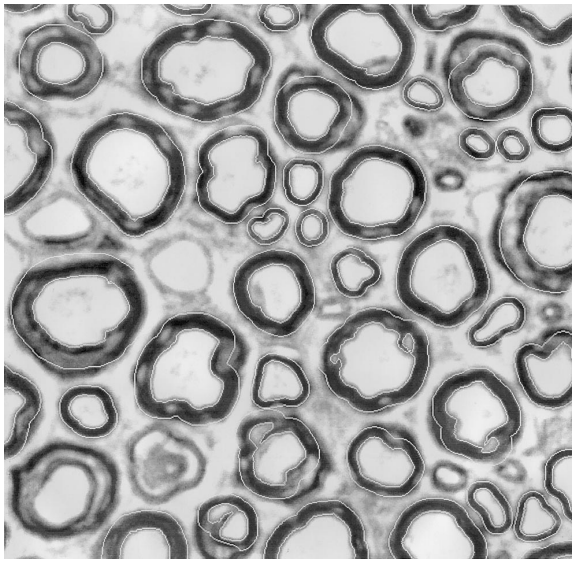

Figure 2.9: Final result of the segmentation algorithm by Romero *et al.*. Image from [RCD+00].

## 2.3 Summary

The segmentation and morphometry applied to microscopy images of the sciatic nerves is still very unexplored in the literature. Also, the studies done so far are regarding images obtained with electron microscopes and not optical microscopy. Electron microscopy images provide more structure detail, but are not able to obtain an image of the full cut of the nerve. Thus, the analysis of optical microscopy images may prove useful, as stated by IBMC researchers. The study of this project will, therefore, concern optical microscopy images rather than the electron ones.

# Chapter 3

# Structure Segmentation and Detection

This chapter describes and compares several segmentation methods applied to the segmentation of light microscopic images of the sciatic nerve. Most of them are present in literature although used for different problems. A new method is also proposed. The results are presented in a visual way for each algorithm. Also, a numeric and objective evaluation and comparison is done in this chapter.

## 3.1 Thresholding Methods

On this section, some algorithms present on the literature will be described, and applied to the four images of the sciatic nerve shown in Figure 3.1. The first three images are relative to a rat without known neuropathologies, whereas the last one was obtained from a nerve of a rat with a crushed sciatic nerve. The methods will be applied to each image, and a small crop of each resulting one will be shown throughout the chapter.

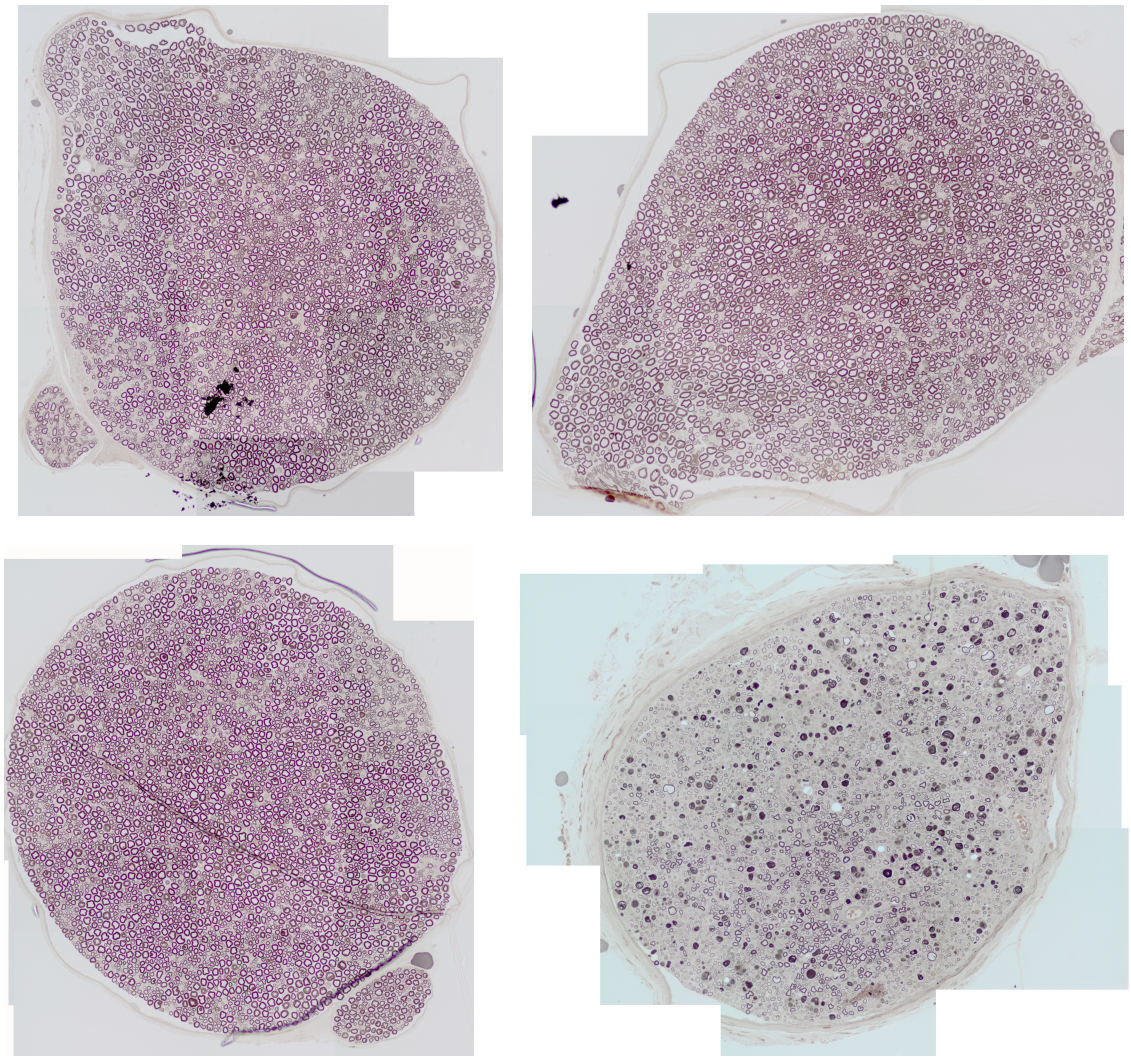

Figure 3.1: Images used to test the algorithms.

### 3.1.1 Otsu Thresholding Technique

The Otsu Thresholding Method, suggested by Nobuyuki Otsu [Ots75], is an unsupervised method widely used for binarization problems. The objective is to find the threshold value that will maximize the separability of the two classes in a grey level image. For each possible value of threshold, the inter-class variance is calculated, and the selected threshold is the one that maximizes this value.

Figure 3.2 shows the results of the algorithm, when applied to four test images. Although the results for the first two pictures may seem acceptable, the algorithm fails to segment and detect structures on the fourth picture.

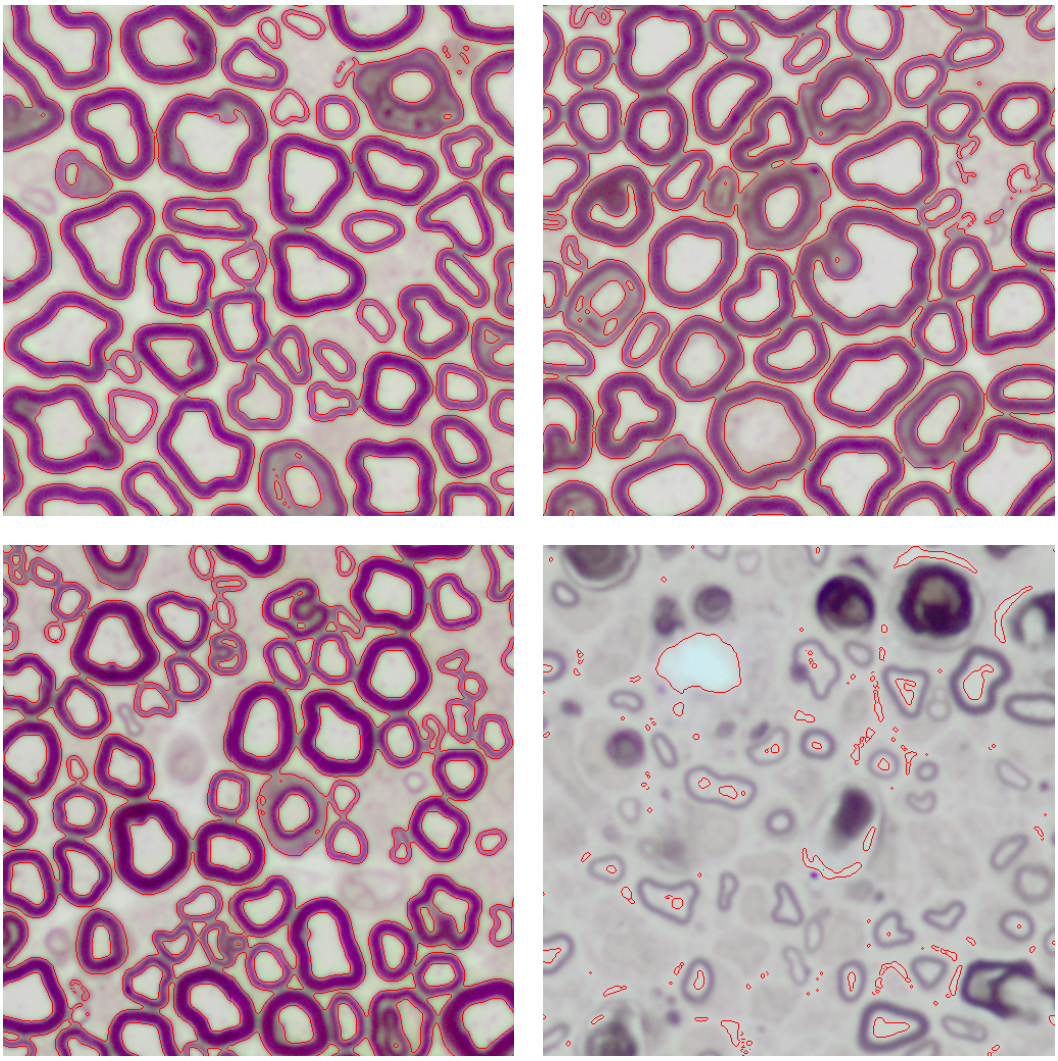

Figure 3.2: Segmentation result of the Otsu Thresholding method.

### 3.1.2 Luminance Thresholding

Khashman and Sekeroglu [KS07] suggested a thresholding method for document enhancement. This is a global single-stage algorithm that, instead of using the peak values in grey-scale histograms, uses the maximum luminance value (brightest point in the image) and mean of intensities in the image to calculate the threshold which best separates the foreground and the background.

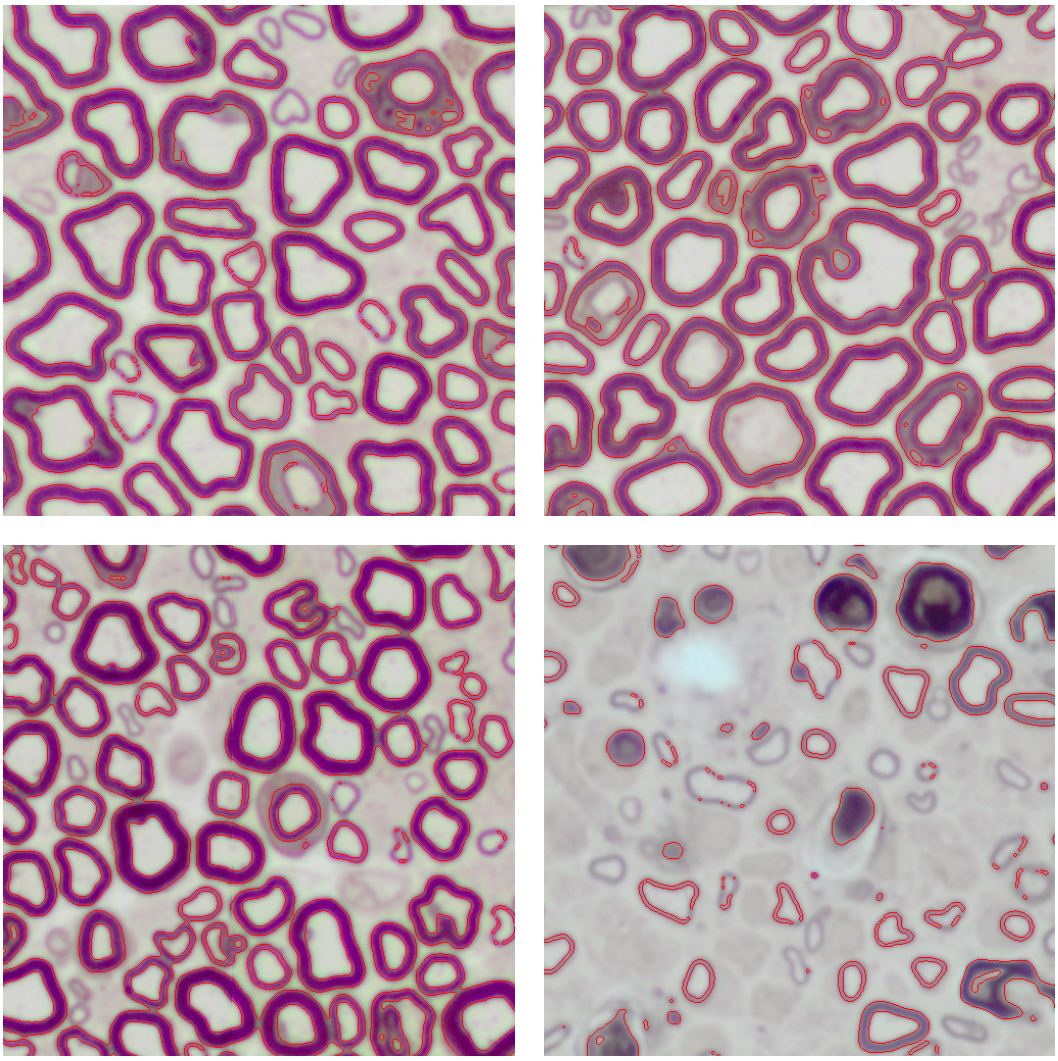

Figure 3.3: Segmentation result of the Luminance Thresholding method.

Figure 3.3 shows the results of the Luminance Thresholding method. Despite the structures that are not detected on the first three images, the segmentation of the remaining structures is quite precise and correct. For the last picture, though, the majority of the detected structures are either false positives or incomplete structures, and there are visibly a few false negatives.

### 3.1.3 Entropic Thresholding

Kapur *et al.* [KSW85] suggested a segmentation algorithm based on the entropy of the two classes, object and background, on the binary image. The objective is to find the threshold value that maximizes the sum of both entropies, using the probabilities of histogram points.

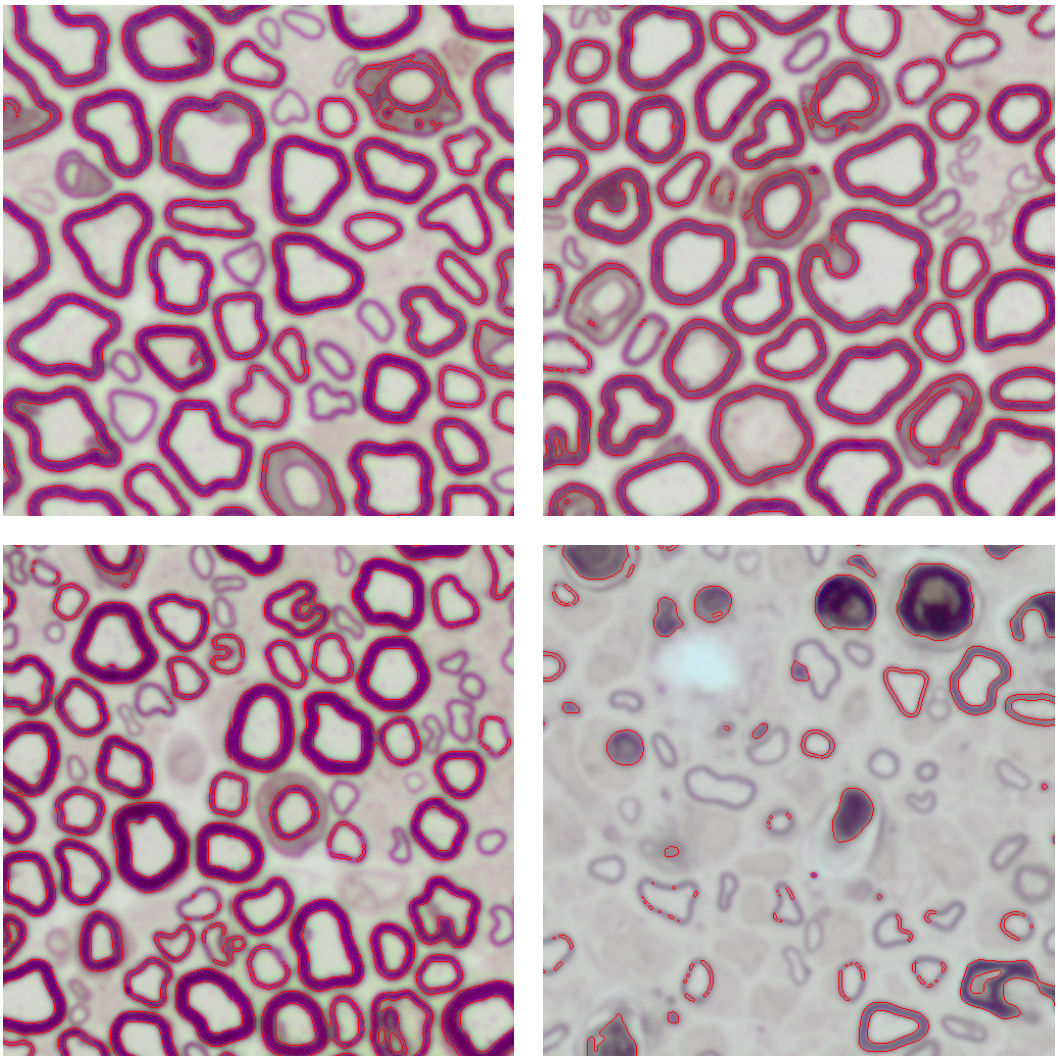

Figure 3.4: Segmentation result of the Entropic Thresholding method.

This algorithm, as shown in Figure 3.4, appears to leave a few structures undetected, on the first three images, unlike the previous ones. Also, the detection on the last image did not improve.

### 3.1.4 Threshold Selection Using Renyi's Entropy

This technique, suggested by Sahoo *et al.* [SWY97] is similar but more robust algorithm than the one described in Chapter 3.1.3, although it is also entropy based. With this method, though, three threshold values are calculated, which may or may not be similar. Using their weighted sums, a final threshold value is calculated.

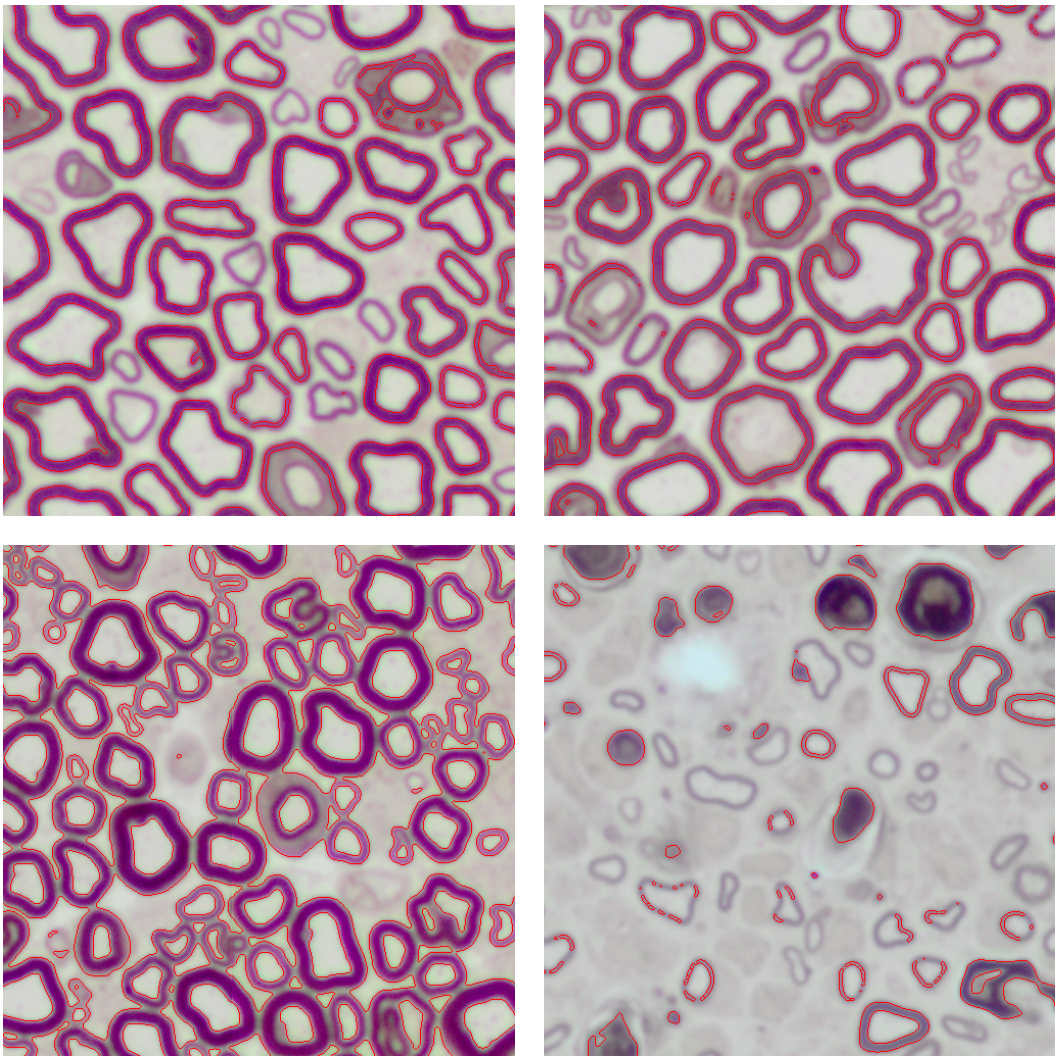

Figure 3.5: Segmentation result of the Renyi's Entropy method.

Figure 3.5 shows the results of this method. On the first two images, there is a significant number of structures that avoid detection. Also, the contours do not capture all of the myelin sheath. On the third image, though, the structures are detected, but there is a visible over-segmentation. On the last image, most structures avoid detection and the ones that are detected are mostly false-positives and incomplete structures.

### 3.1.5 Tsallis' Entropy

Albuquerque *et al.* [dAEMdA04] suggested another algorithm similar to the maximum entropy sum. This method calculates the optimum threshold value, by maximizing the Tsallis' entropy, which is calculated using probability distributions for the two classes, object and background. The Tsallis' entropy technique is parameter dependant, which allows method tweaking to better fit the problem at hand.

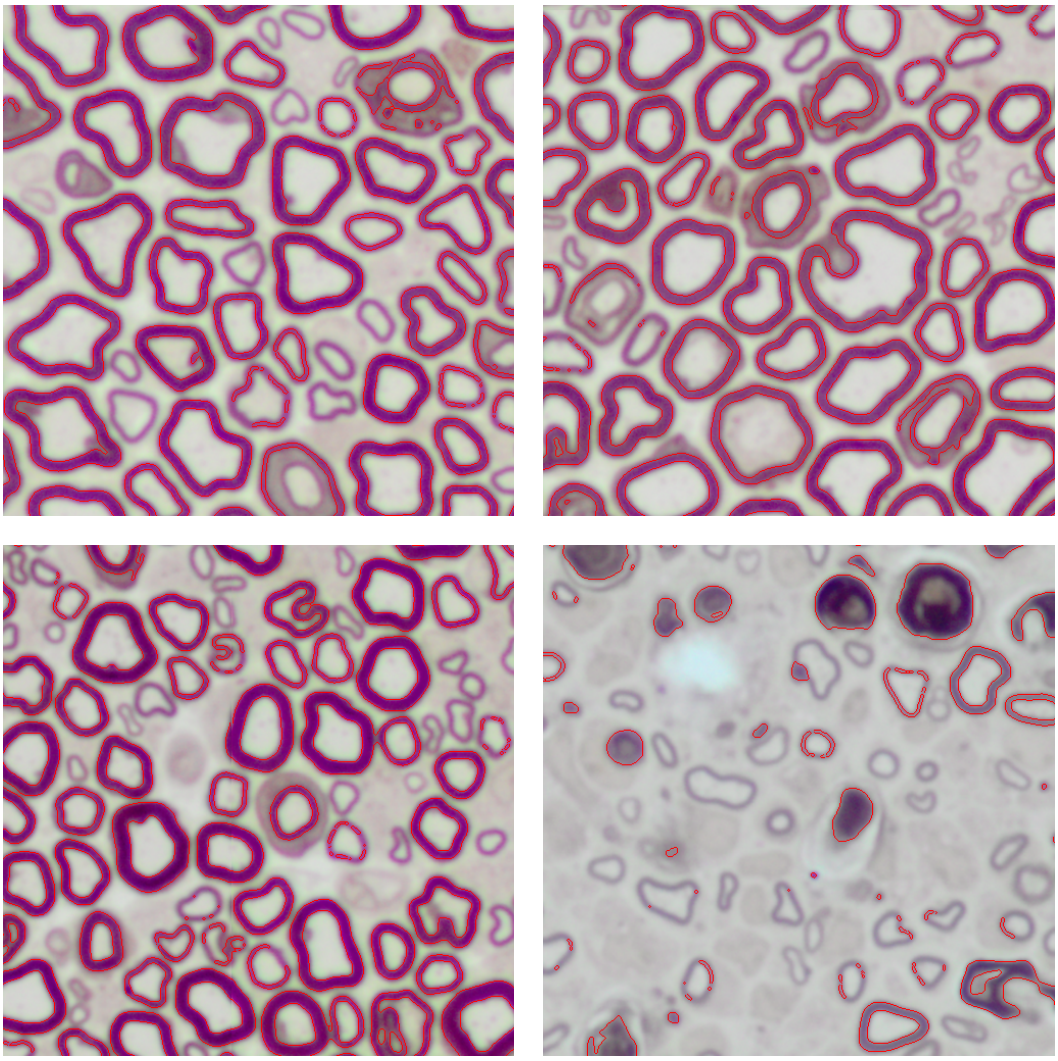

Figure 3.6: Segmentation result of the Tsallis' Entropy method.

The detection and segmentation on the first three images with this algorithm, as shown on Figure 3.6, is fairly poor. The algorithm also does not solve the problem on the fourth image.

### 3.1.6 Gaussian Smoothing

Tsai [Tsa95] suggested an iterative method based on Gaussian smoothing of the grey-level histogram to remove false peaks and valleys, in order to find the valley that presents the best separation of the two classes, object and background. The algorithm stops smoothing the histogram when a single valley exists, which is then considered to hold the optimum threshold.

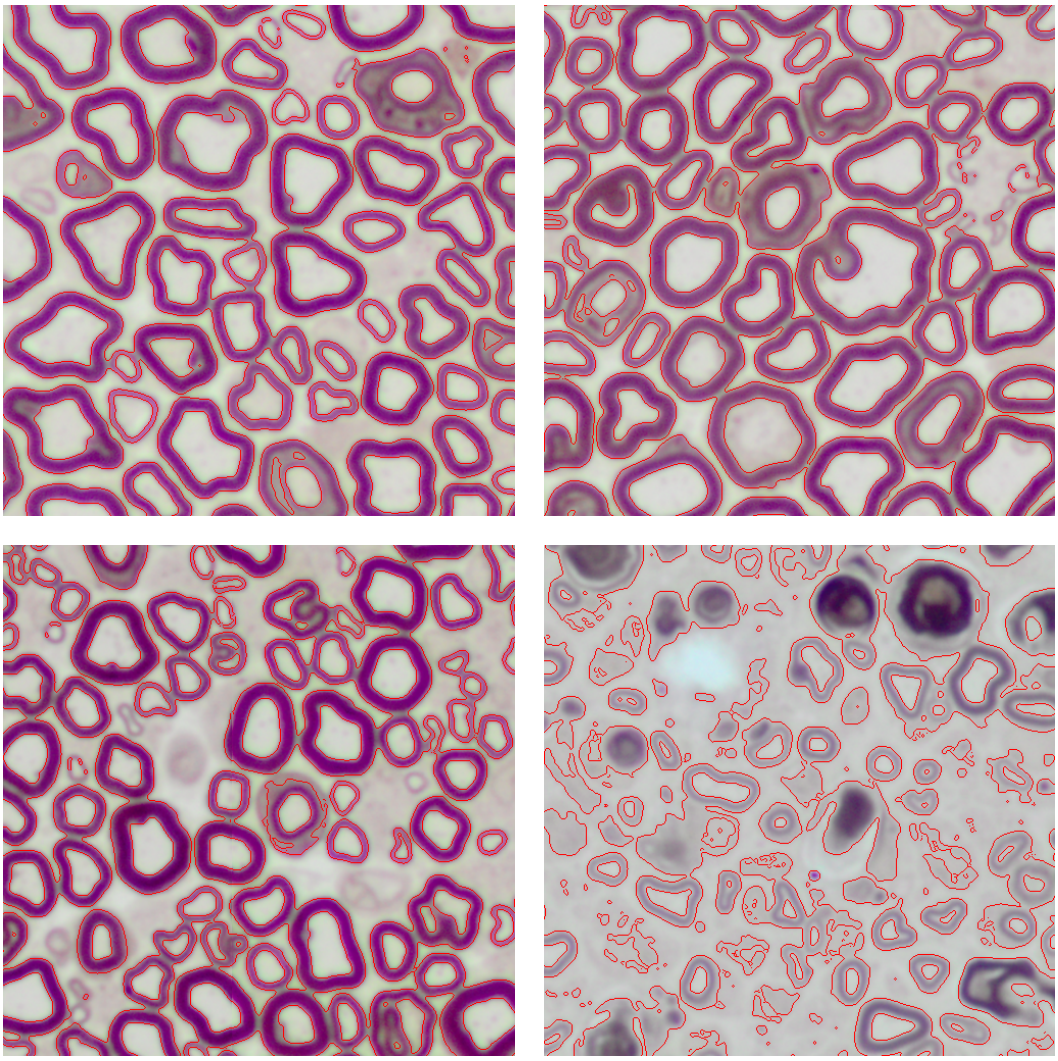

Figure 3.7: Segmentation result of the Gaussian Smoothing method.

Figure 3.7 shows the results of the application of the Gaussian Smoothing algorithm. This algorithm detects nearly all of the structures, although it may suffer from some over-segmentation. Disregarding that, the algorithm behaves the same way with all the images even though this flaw is more evident on the last one.

### 3.1.7 Binarization Based in Line Spacing and Thickness (BLIST)

Pinto *et al.* [PRGC11] introduced an algorithm for music score binarization, BLIST. This algorithm selects the optimum threshold by attempting to maximize the number of staff lines detected with a certain line thickness and spacing.

This problem, although far too different from the sciatic nerve image segmentation, has two similarities. The myelin sheaths are darker than the rest of the image, similar to the music staff. Also, since BLIST analyses vertical windows of the image, it looks as if

the image is comprised of thick, dark, horizontal and distorted lines separated by a lighter space, which can either be the axon or the background, similar to the musical staff line spacing. Figure 3.8 shows some examples of such event.

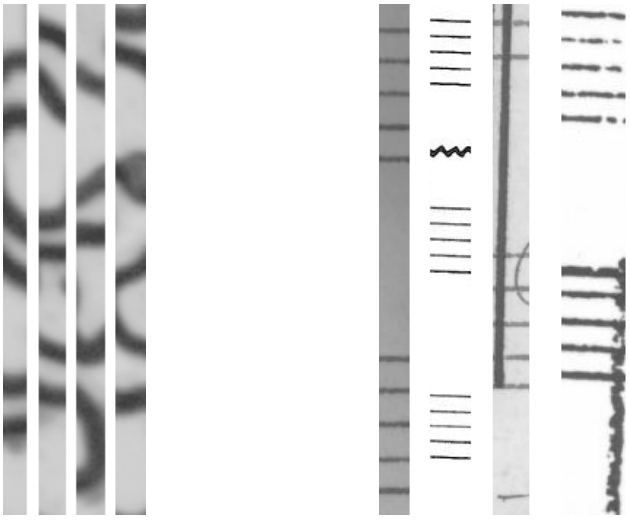

Figure 3.8: Comparison between Sciatic Nerve and Music Staff Windows.

BLIST results are shown on Figure 3.9. For the first three images, the detection is good but there is still some over-segmentation. On the last image, though, the structures are still detected and there is significantly less over-segmentation than on the algorithm described on Section 3.1.6.

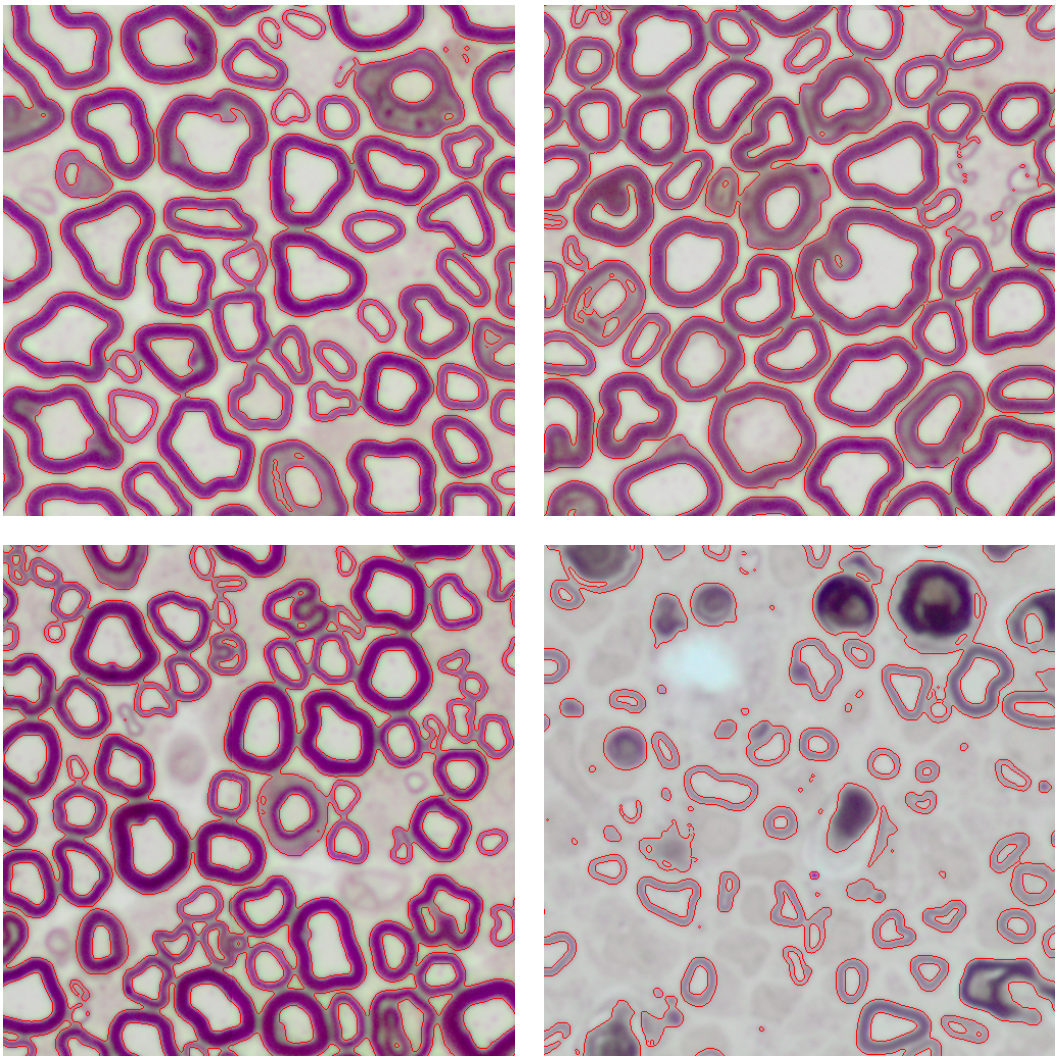

Figure 3.9: Segmentation result of the BLIST method.

### 3.1.8 Euler Number Optimization

This technique, introduced in this work, uses some of the *a priori* knowledge previously described regarding the composition of the structures. Each image is comprised of hundreds or thousands of axons and each of them is surrounded by a darker layer, the myelin sheath. If the myelin sheath is represented as white and both the axon and the background are considered as black, the binary image is comprised of white objects with a single black hole. Figure 3.10 shows a crop from an original image and its respective segmentation result.

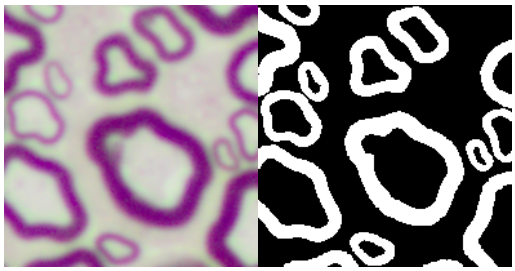

Figure 3.10: (a) A crop from an original image; (b) Binary representation of the image;

Since two axons never overlap themselves in the image, although they can be very close together, each structure, comprised of an axon and its surrounding myelin sheath, can be considered an object with exactly one hole. If an object has less or more holes, either it is due to incorrect segmentation results or it is a strange structure and should not be considered.

The Euler Number of an image is the number of objects in that region minus the total number of existing holes. If a region containing a single axon is considered, the number of objects would be one, and the same for the holes. That means the Euler Number of a valid structure is always zero, since each object has exactly one hole.

The objective of this methodology is, therefore, to find the threshold that maximizes the number of structures in the image with Euler Number equal to zero which, *a priori*, represents detecting as many axons as possible. In order to improve the execution time, the image can be cropped and the threshold calculated using only the partial image. This means the threshold selected is the one that maximizes the number of structures obtained in the partial image, which may be different from the one that would maximize it for the whole image. Therefore, the cropped window needs to be big enough so there is only a slight difference, even if the run time reduction is not as significant as with a smaller window. The results for both the full image and a sampling window of 800 x 800 will presented throughout the document.

A simple pseudo-code for this algorithm is:

```
For each possible threshold value:
- Step 1: Calculate the Euler Number of each object in the
binary image.
- Step 2: Calculate the amount of objects with Euler Number
equal to zero.
- Step 3: If the value computed in Step 2 is higher than
the current highest value, then this is the best threshold
so far.

Finally, binarize the image using the threshold that maximizes
```

```
the number of captured objects with Euler Number equal to zero.
```

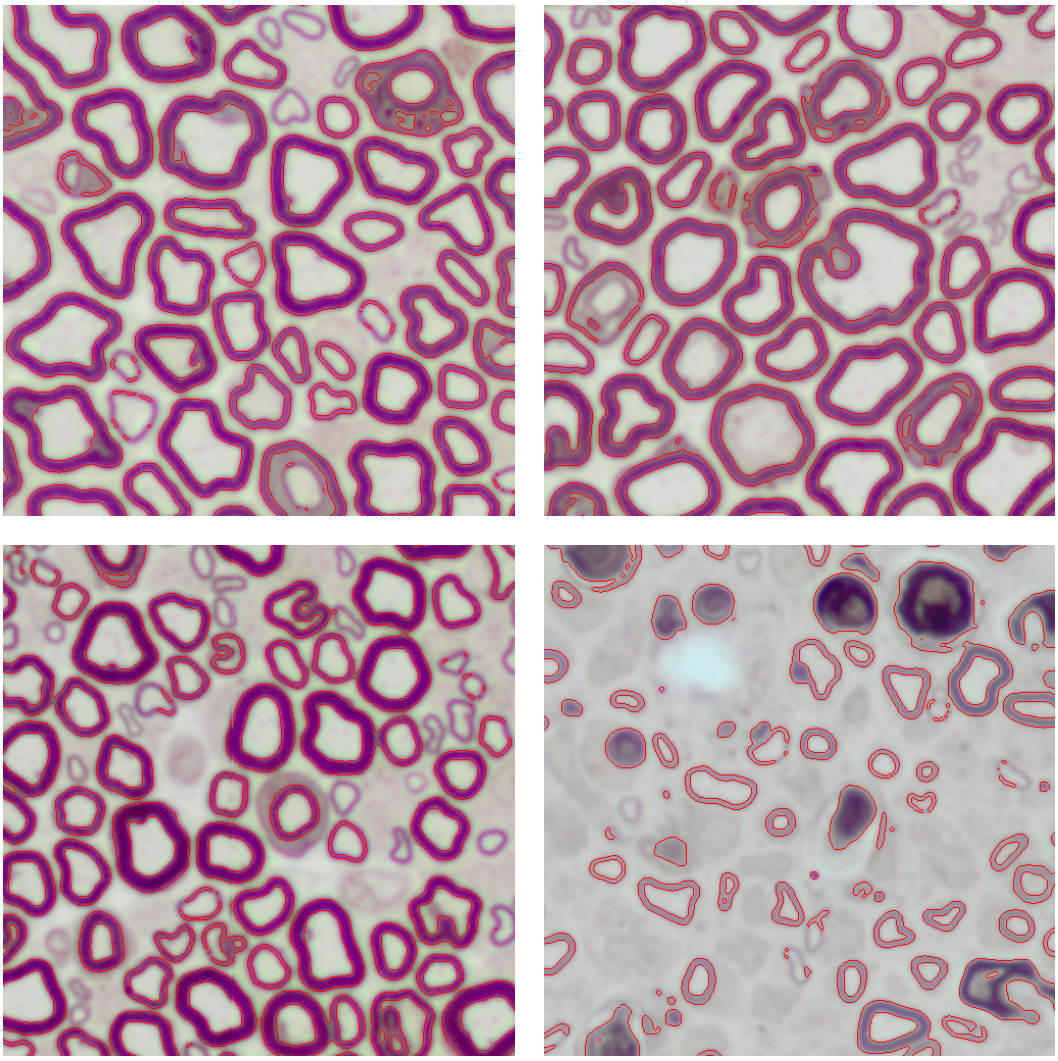

Figure 3.11: Segmentation result of the Euler Number Optimization method.

Figure 3.11 shows the results of this algorithm. The contours are fairly good for all the images, but some structures escape detection, specially on the first three images.

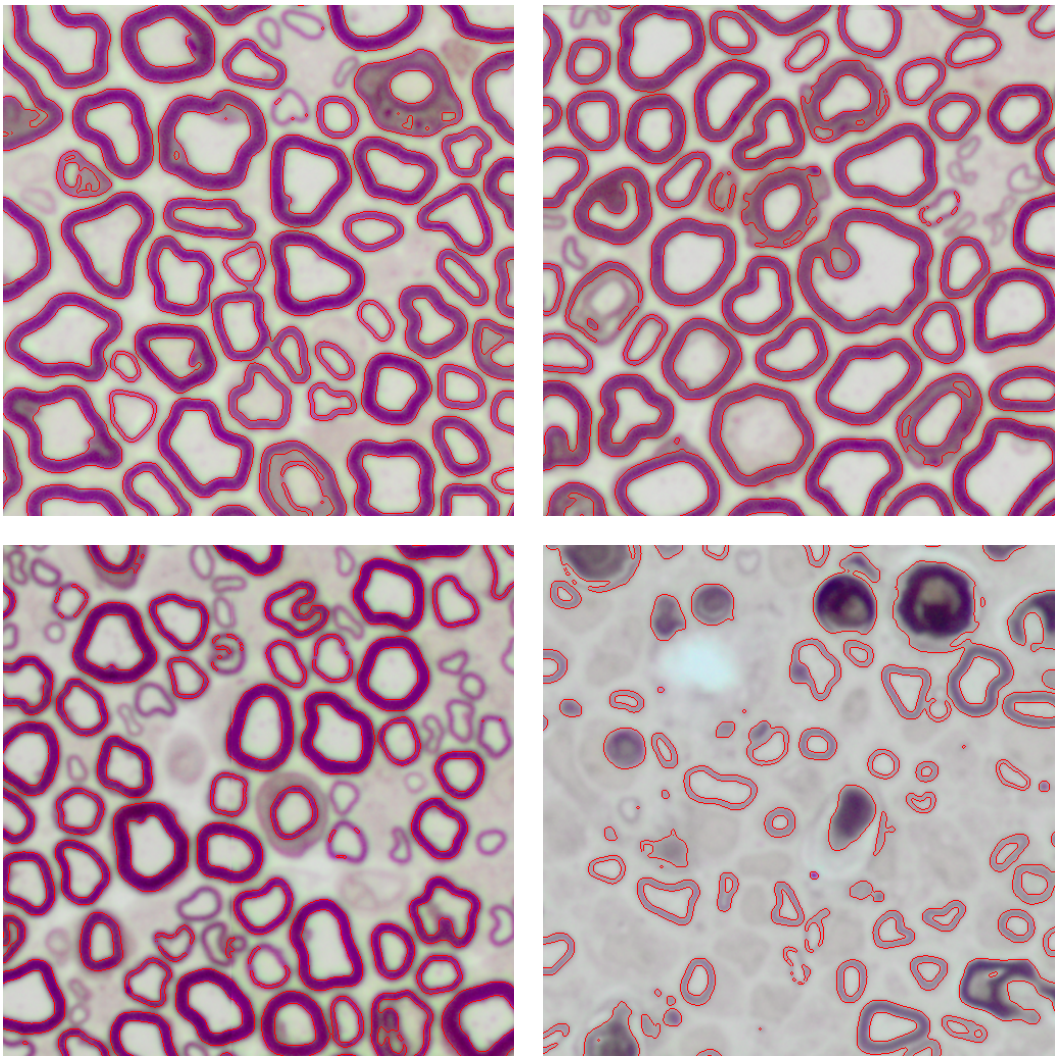

Figure 3.12: Segmentation result of the Euler Number Optimization method, with a sampling window.

Figure 3.12 shows the results of the algorithm using the sampling window previously mentioned. Visually, the results do not change significantly.

## 3.2 Comparative Results

In order to do a more objective comparison of the algorithms, a ground truth was established. The original images are far too big to be manually segmented, so they were cropped first. The resulting images were validated by a researcher from IBMC, and are shown in Figure 3.13.

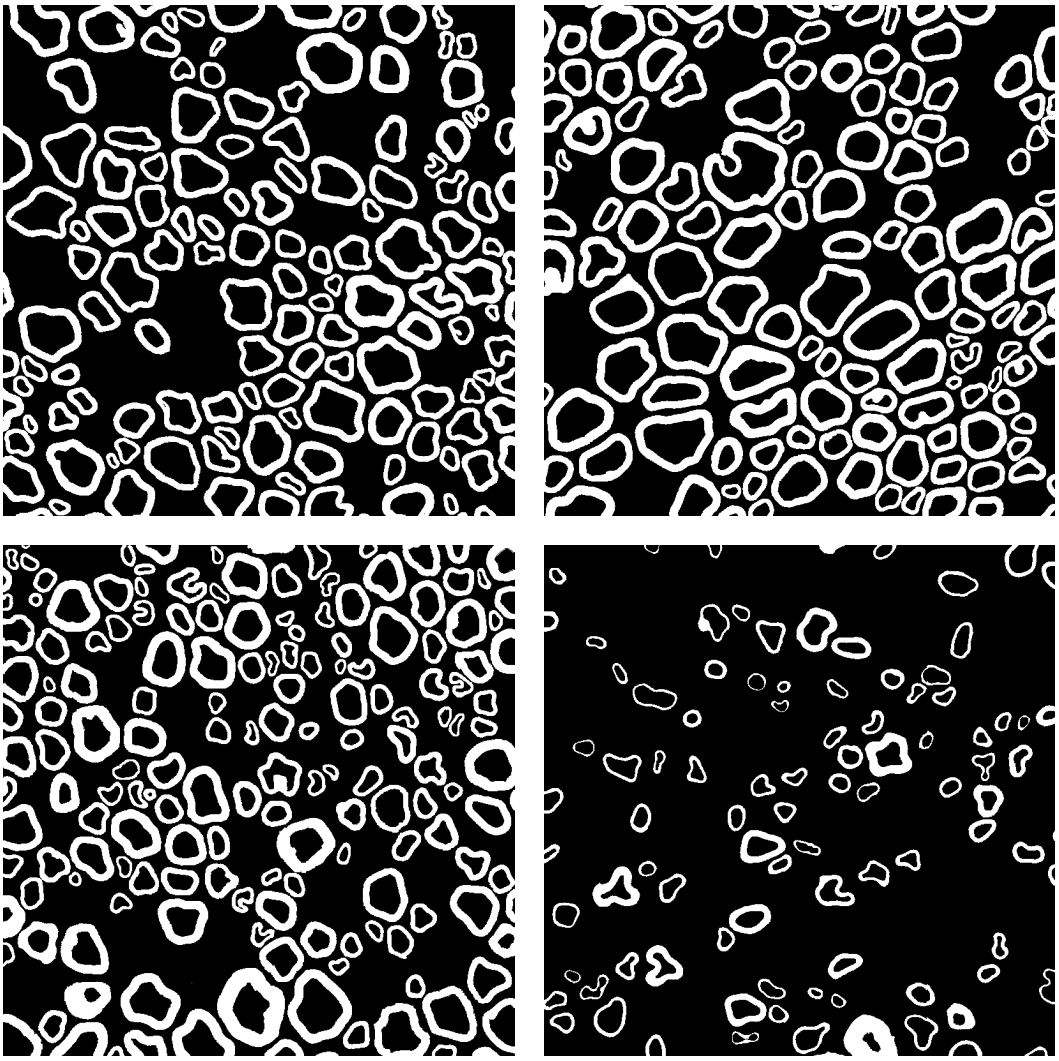

Figure 3.13: Images used as ground truth.

The binary images resultant from each algorithm were compared to the ground truth bitwise, and the percentage of matching pixels are shown in Table 3.1. A valid structure will always have one and only one hole, meaning its Euler Number will be zero. Table 3.1 also shows the number of objects in the original (not cropped) images following this rule that were detected. It is important to note that two structures merged together (false-negative) and artefacts with a single hole (false-positives) are excluded and included, respectively, in these values. This table also shows the time it takes for each algorithm to run. The algorithms are implemented in Matlab® R2010a, and the tests were run using a Core i5 330M, HDD Sata 5400 rpm and 4GB RAM.

The crop size used on this images is 800px x 800px, while the one used for the images in the previous sections was 500px x 500px. Since the locations were picked randomly, this explains the apparent differences between the previous sections and the ones showed on Table 3.1.

The algorithm with the best average results is the Luminance Thresholding, immediately followed by the new algorithm suggested in this work with a difference of 0.3% of correctly segmented pixels. The segmented images, were presented to the IBMC specialist who found the segmentation results satisfactory. This algorithm also detects high number of valid objects.

In some cases, the Euler Number Optimization algorithm detects less valid objects than the Luminance Thresholding technique, which is due to using a sampling window to calculate the threshold, instead of using the whole image. Even though, the Euler Number Optimization method has the best average detection. Naturally, this event does not occur when the whole image is used, as the table shows. Although the results may worsen when using a sampling window, the execution time of the algorithm greatly improves. In cases where the accuracy of the results is more important than the run time, it may be best to use the whole image. Otherwise, the sampling window may be worth some consideration.

The number of structures detected may not be of extreme importance to compare the algorithms presented. For example, the Euler Number Optimization algorithm aims to use the threshold that maximizes the number of structures with Euler Number equal to zero, thus having, unless using sampling windows, always the maximum possible value amongst the algorithms. These values are important, though, when comparing them to the software-aided process used by IBMC at the moment, and when comparing the estimated number of structures in the whole image. These numbers, also present in Table 3.1, are an estimate axon count, since manually counting all of the structures in the image would take too long.

| | | Otsu | Luminance Thresholding | Entropic Threshold | Renyi's Entropy | Tsallis' Entropy | Gaussian Smoothing | BLIST | Euler Number Optimization (crop) | Euler Number Optimization | |
|---|---|---|---|---|---|---|---|---|---|---|---|
| Correct Pixels | Image 1 | 82.9% | 86.9% | 85.3% | 85.3% | 84.9% | 84.2% | 83.4% | 86.4% | 86.9% | |
| | Image 2 | 80.9% | 89.3% | 85.6% | 84.8% | 85.2% | 82.3% | 83.1% | 89.2% | 89.1% | |
| | Image 3 | 84.0% | 87.4% | 85.7% | 79.5% | 85.3% | 86.0% | 83.7% | 84.4% | 86.6% | |
| | Image 4 | 12.2% | 90.3% | 89.3% | 89.4% | 89.0% | 63.0% | 83.0% | 88.0% | 90.0% | |
| | Average | 65.0% | **88.5%** | 86.5% | 84.8% | 86.1% | 78.9% | 83.3% | **87.0%** | 88.2% | Manual |
| Valid Objects | Image 1 | 1343 | 2866 | 2364 | 2364 | 2259 | 1760 | 1490 | 2559 | 2887 | 3907 |
| | Image 2 | 648 | 2058 | 2098 | 1975 | 2026 | 764 | 850 | 2455 | 2493 | 5142 |
| | Image 3 | 1279 | 2696 | 2825 | 631 | 2785 | 1782 | 1232 | 2571 | 2923 | 4234 |
| | Image 4 | 119 | 1755 | 1414 | 1469 | 1323 | 1017 | 2021 | 2161 | 2175 | 2641 |
| | Average | 847 | **2344** | 2175 | 1610 | 2142 | 1331 | 1398 | **2437** | 2620 | |
| Run Time (s) | | 1 | 3 | 8 | 21 | 8 | 9 | 492 | 56 | 1714 | |

Table 3.1: An objective comparison of the presented algorithms.

| | White Pixels | Black Pixels |
|---|---|---|
| Image 1 | 29.8% | 70.2% |
| Image 2 | 34.1% | 65.9% |
| Image 3 | 32.1% | 67.9% |
| Image 4 | 9.2% | 90.8% |

Table 3.2: A baseline for the previous results.

Table 3.2 presents a baseline for the previous results. The percentage of white and black pixels is show for each of the ground truth images. Since a high percentage of the pixels in the image are black, a blind algorithm that would classify every pixel as black would have a relatively high percentage of correct segmented pixels, although it would not detect any structure for posterior measurement. These values may be used as reference for analysing the results presented in Table 3.1.

## 3.3 Summary

The results achieved with the previous algorithms are satisfactory, since they present a significant improvement when compared to the currently adopted processes, as mentioned by a researcher from IBMC.

It is also important to note the number of assumed as valid structures the algorithms detect after the binarization step.

Although the values obtained with the algorithms are still far from the ones estimated by the IBMC researcher, the improvement is already significant taking into account that only two hundred and fifty structures are analysed with the IBMC manual, albeit software-aided, processes.

A problem with the segmentation methods tested is that too many structures are segmented as merged, and some are incorrectly considered as valid. Splitting the merged structures and removing the invalid ones can improve the number of valid structures to analyse, thus increasing the accuracy of the measurements.

# Chapter 4

# Segmentation Improvement

This chapter presents a methodology to improve the segmentation results obtained in the previous chapter, by splitting the merged structures and ignoring the odd structures that may lead to incorrect characteristics measurement in later stages of this work.

## 4.1 Merged Structures Split

Although two axons, or their myelin sheaths, never overlap, it may happen that the thin patch of background separating them is not segmented as background, but as myelin. Such cases are shown in Figure 4.1.

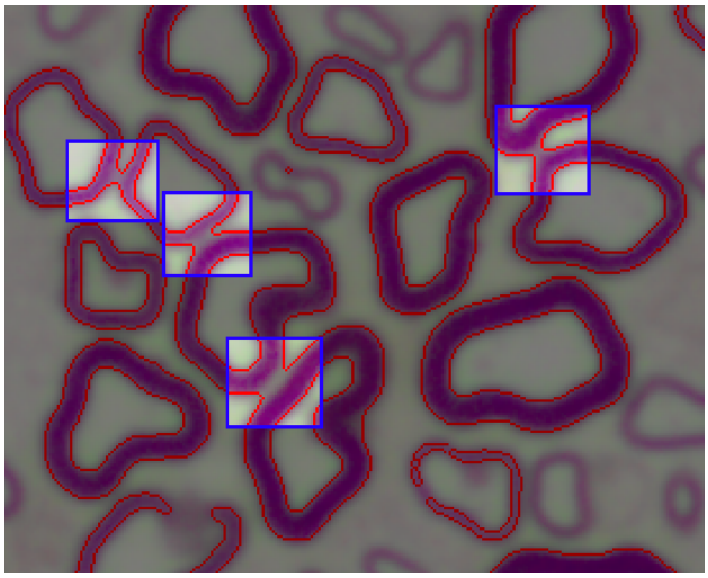

Figure 4.1: Example of merged structures.

Depending on the algorithm used for the segmentation, this may happen with a higher or lower frequency. All the algorithms tested and described in Chapter 3 created such cases, and the correction of this segmentation error may significantly increase the number of structures considered as valid. For that reason, a postprocessing method that splits the merged structures may increase the accuracy of the final measurements.

An algorithm commonly used in the literature for geological and histological images is the watershed segmentation method [LTA02]. This algorithm, initially suggested by Buecher and Lantuejoul [BL79], was later turned into an "immersion-based" algorithm by Vincent and Soille [VS91] and the following analogy can be used to explain its behaviour.

A grey scale image can be considered as a topographical relief, where the value of each pixel represents the elevation of that region. Water is immersing from the bottom of the relief, which is gray-level 0. Each time the water reaches a local minimum, it is considered as a new catchment basin. Eventually, as the water level keeps rising, two neighbour catchment basins will meet each other, and a dam is created so that the water from the two places will not merge. When the water-level hits it maximum height, the algorithm ends, and the edges of the union of all dams form the watershed segmentation. The marker-based watershed segmentation follows the same principles, but only regions with a marker may be considered as catchment basins.

The objective of the application of this algorithm in this specific problem is to split merged structures. To do so, the objects with more than one hole, which are potentially merged structures, were selected and the holes were used as markers. The background is also marked. The myelin sheath was turned into a gradient, so that the outer borders have a higher value in grey-scale than the rest of the myelin sheath. As the water level rises, it will eventually reach the outer and higher part of the myelin sheath from the two merged structures. Eventually, the water from the two catchment basins will join, and a dam is created. That dam is the border between the two structures, and allows for their separation. Figure 4.2 illustrates this with the holes and background in black (markers), and the myelin sheath with a gradient.

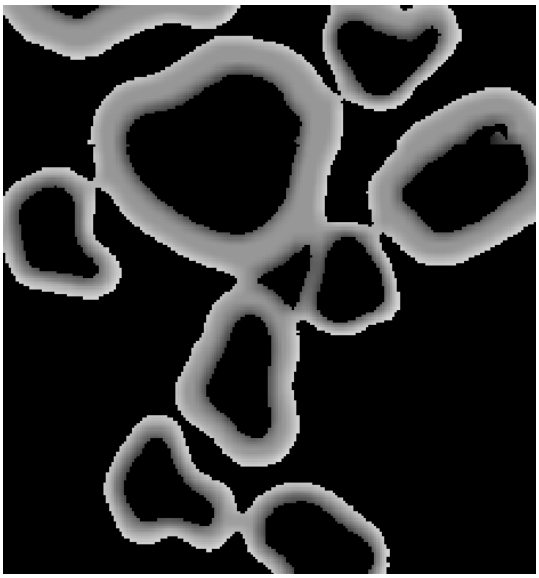

Figure 4.2: Example of an image ready to be used as input for the watershed algorithm.

Figure 4.3 shows the result of the application of the watershed algorithm. The red rectangles represent the correctly effectuated splits. The blue rectangle highlights a case where the watershed fails, due to a incorrectly mark. As is visible in Figure 4.2, that patch of background between the three structures is marked as a catchment basin, which is why the algorithm fails.

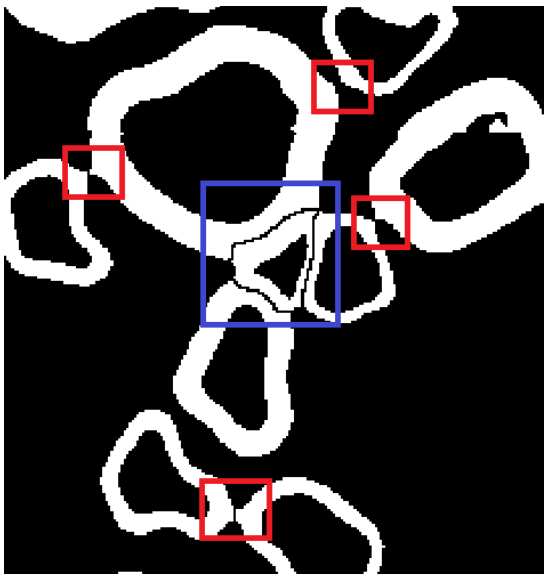

Figure 4.3: Results of the watershed algorithm.

Another segmentation error the watershed sometimes introduces is related to image artefacts, which can have various sources. Figure 4.4 shows an example, caused by a dye stain.

Figure 4.4: Error in segmentation - Segmenting a dye stain.

## 4.2 Invalid Structures Removal

As previous stated, various sources of errors may lead to the acceptance of odd structures in the segmentation phase, and the merged cell split may introduce new ones. The different kinds of errors are shown in Figure 4.5.

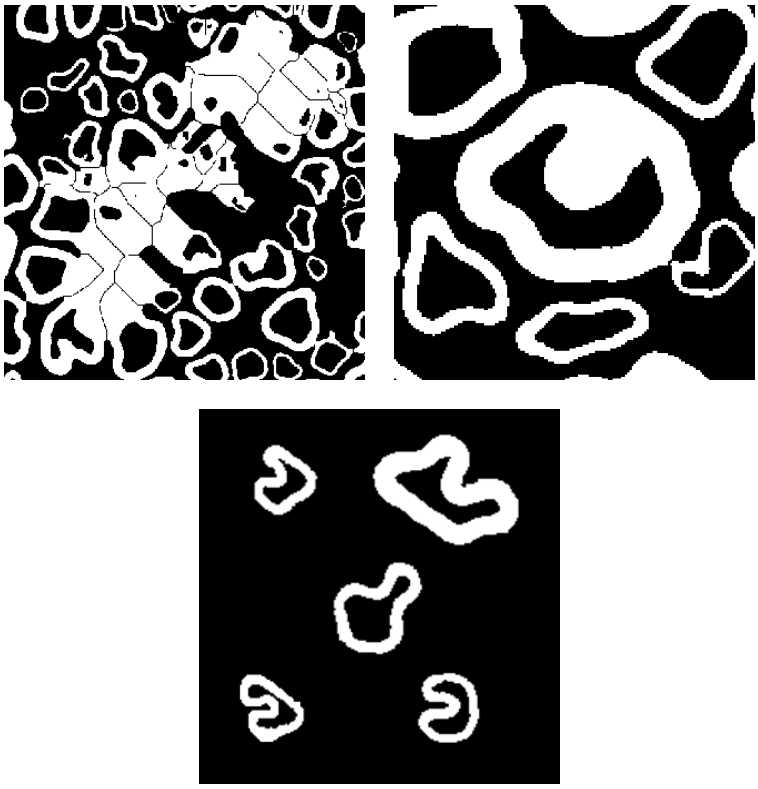

Figure 4.5: (a) Some image artefacts may be considered as a structure; (b) The cut may, sometimes, catch a glimpse of the Schwann Cell; (c) During the preparation of the cut, some structures may twist so much they should not used for G-Ratio calculations.

These structures need to be ignored, otherwise they can lead to significant disturbance in the measuring results, depending on their frequency. Therefore, some work was done regarding this step of the algorithm in an attempt to develop a method to detect and eliminate such structures.

To do so, some characteristics of those structures are useful to keep in mind.

As seen in Figure 4.5a, artefacts may have the most odd looking forms but still be considerer as valid structures. A way to detect these erroneous objects may be to compare the inner and outer borders' forms. The difference is commonly very obvious.

There are Schwann Cells alongside the axons throughout the sciatic nerve. When gathering a longitudinal cut of a random section in the nerve, many Schwann cells will also be cut and they will show up in the image, as seen in Figure 4.5b. These structures are also ignored by the researchers at IBMC during the measurements, due to the method used to calculate the G-Ratio, which will be explained in Chapter 5.

Also, due to dehydration during the staining process or simply due to the pressure during the sectioning of the sciatic nerve, the cells tend to shrink irregularly along the border. In some cases, such as the ones shown in Figure 4.5c, the structures become so

twisted that the researchers tend to ignore them, since the alteration of the form might indicate the results will be adulterated due to the mentioned process problems.

To eliminate these cells automatically, it is necessary to find one or more measures of "structure's oddness". These measurement needs to clearly separate the valid axons from the ones that should be ignored. After measuring the oddness of a structure, the ones that score above a certain threshold are ignored, and the others are kept.

Unfortunately, the attempt to find or develop such a measurement did not succeed, so this step was reduced to a simple, and previously mentioned, action: removing all the structures that do not have one and only one hole. In order to do that, the object property Euler Number is used. And stated before, an object with a single hole have Euler Number equal to zero. All the other structures were ignored.

## 4.3 Summary

The segmentation done on the previous steps has errors that may cause some deviations in the final calculations of the measures. The watershed algorithm, by splitting merged structures, increases the number of structures, but introduces new kinds of errors. For this reason, it is essential that an algorithm for invalid structure removal is developed in this stage, that not only removes structures with no hole, or more than one, but also structures that would, in a manual process, be ignored by the researcher.

Since the removal of the invalid structures is not implemented, the influence of the methods described in this chapter on the final results will be discussed in Chapter 6.

# Chapter 5

# Morphometry

This chapter will describe the characteristics measurement from binarized images. To avoid the propagation of the errors from the previous steps, the method is applied to the ground truth images presented on Chapter 3. The results for the whole process will be described on Chapter 6.

## 5.1 Methodology

The G-Ratio, as previously stated, is the ratio between the diameter of the axon and the diameter of the whole structure, the axon plus the myelin sheath. Measuring the diameter is not straightforward, though. The structures are not circular, which means that the value of the diameter is different depending on the position of the axis used to measure the diameter.

The method used by IBMC researchers assumes that a structure resemblances a circle with hollows and prominences, as well as that the outer border of the myelin sheath closely resembles the inner border. Some structures, as show in previous chapter, are too odd for this assumption to be possible, so they are ignored when selecting the structures to measure. Instead of measuring the diameter, it is calculated through mathematical formulas for circles. To reduce the error from the assumption, it is calculated using both the perimeter and the area, and then the average is used to calculate the G-Ratio.

Using the formula for the perimeter, $P$, of a circle,

$$P = 2 * \pi * r \tag{5.1}$$

we can calculate the diameter, $D_p$, as:

$$D_p = \frac{P}{\pi} \tag{5.2}$$

Using the formula for the area, $A$, of a circle,

$$A = \pi * r^2 \tag{5.3}$$

we can calculate diameter, $D_a$, as:

$$D_a = 2 * \sqrt{\frac{A}{\pi}} \tag{5.4}$$

The diameter, $D$, is the mean of the two values calculated previously:

$$D = \frac{D_a + D_p}{2} \tag{5.5}$$

The diameter of the axon, $D_{ax}$, and the diameter of the structure, $D_{st}$, are both calculated using the previous formulas. The G-Ratio of each structure, $GR_s$, is the ratio between $D_{ax}$ and $D_{st}$ and for the whole image is the mean of all the structures G-Ratios. For an image with $n$ structures, the G-Ratio, $GR$, is calculated as:

$$GR = \frac{\sum_{i=1}^{n} \frac{D_{ax[i]}}{D_{st[i]}}}{n} \tag{5.6}$$

## 5.2 Results

To validate the results of this algorithm, a manual measurement was done by an IBMC expert researcher, using the segmentation ground truth images. The images contain incomplete structures, in the borders, and some whose myelin sheath are too twisted. Those structures were ignored and the morphometry process was applied only to the other structures. Figure 5.1 shows the images used for both the manual and automated processes. The ones with the axon painted as grey, and the ones whose axons are outside the cropped zone, were ignored. The red arrows indicate structures that were considered in the process, but turned out to have a low G-Ratio, which indicates that even the manual process will consider some outliers.

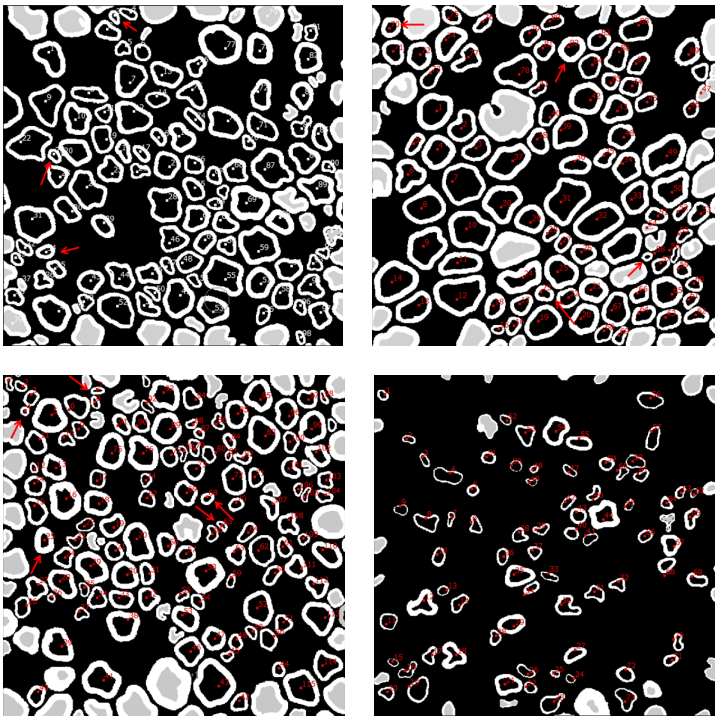

Figure 5.1: Image dataset for the morphometry problem.

All the structures in each image were manually, albeit software-aided, measured by a researcher from IBMC, and the G-Ratio for each image was calculated. The previously described automatic algorithms were applied to the same structures and the results are displayed on Table 5.1.

| | Manual Measurement | Automated Measurement |
|---|---|---|
| Image 1 | 0.657 | 0.650 |
| Image 2 | 0.658 | 0.650 |
| Image 3 | 0.642 | 0.634 |
| Image 4 | 0.701 | 0.675 |

Table 5.1: Comparison between the manual and automated morphometry technique G-Ratio results.

This represents a Mean Squared Error of about 0.007, which represents 1% of the average of the G-Ratio values on the analysed images.

According to the researchers, the bigger an axon is, the higher its G-Ration tends to be. Plotting the diameter of the axon against its G-Ratio, the best fitting line should, therefore, have a positive slope. The plots for each image are shown on Figure 5.2.

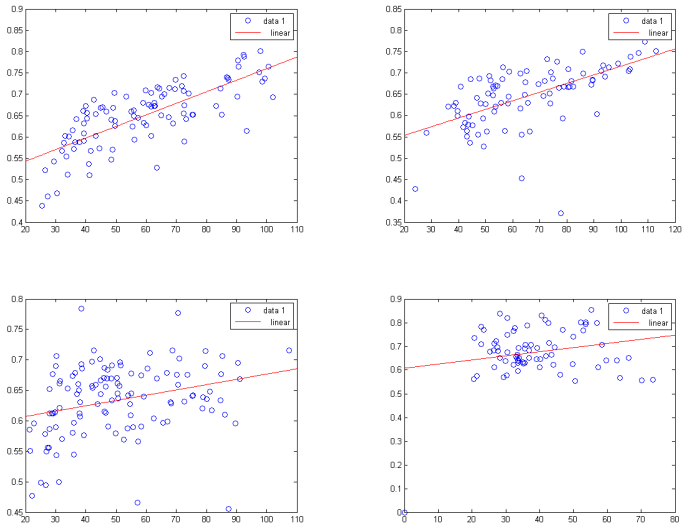


Figure 5.2: (a) Image 1; (b) Image 2; (c) Image 3; (d) Image 4; G-Ratio graphic plots for each image. On the *xx* axis, there is the diameter of the axon and on the *yy* axis the axon G-Ratio.

## 5.3 Summary

The manual and the automated approaches use the same formulas to calculate the G-Ratio, but the measurements of the perimeter and area of each structure are done differently, hence the differences in the values shown. Although there is a difference, the automated process output is very similar to the manual one.

# Chapter 6

# Results

In this chapter, the results for the entire process of segmentation and characteristics measurement are described. The results are presented in next two tables. Table 6.1 shows the measurement of the G-Ratio by each algorithm, for each image. The manual measurements made by an expert are also presented in this table. For each algorithm, the mean squared error is calculated, using the manual measurements as ground truth. These values were calculated both with and without the intermediate step, the previously described segmentation improvement. As expected, due to the lack of elimination of the false positive detections, the outliers introduced by the watershed separation end up worsening the correctness of the G-Ratio measurements in most of the cases.

The G-Ratio was calculated not only using the mean of all the values, as stated on the previous chapter, but also as the median of all the values. The median tends to be a more robust method when dealing with outliers. Since the segmentation improvement step introduced outliers, this method was tried. As can be seen in the table, in some cases the results improved when applying the segmentation improvement step and using the median instead of the mean value.

The method that presented the best results in the segmentation step, the Luminance Thresholding method suggested by Khashman and Sekeroglu, also provided the best results for the process as a whole. For this algorithm, the segmentation improvement step improves the final measurements accuracy when calculated using the median value.

Table 6.2 shows the number of structures detected with each algorithm, with and without the segmentation improvement step and compares it with the values obtained by the IBMC researchers with the manual process. The table shows that the structure splitting algorithm suggested in Chapter 4 greatly increases the amount of detected structures, although this number would decrease if the removal of imperfect structures was implemented. Nevertheless, this is still an objective metric worth mentioning and it is worth notice that the algorithm that has the lowest MSE after the segmentation phase is the Euler Number Optimization algorithm, and that the Luminance Thresholding has the lowest

MSE after the segmentation improvement step.

| | | | Otsu | Luminance Threshold-ing | Entropic Threshold | Renyi's Entropy | Tsallis' Entropy | Gaussian Smooth-ing | BLIST | Euler Number Optimization (crop) | Euler Number Optimization | Manual Measure-ments |
|---|---|---|---|---|---|---|---|---|---|---|---|---|
| Mean | Without Segmentation Improvements | Image 1 | 0.619 | 0.686 | 0.698 | 0.632 | 0.624 | 0.667 | 0.624 | 0.667 | 0.688 | 0.689 |
| | | Image 2 | 0.608 | 0.681 | 0.681 | 0.614 | 0.619 | 0.698 | 0.619 | 0.698 | 0.699 | 0.657 |
| | | Image 3 | 0.625 | 0.679 | 0.706 | 0.643 | 0.620 | 0.699 | 0.620 | 0.699 | 0.697 | 0.645 |
| | | Image 4 | 0.052 | 0.642 | 0.646 | 0.276 | 0.456 | 0.533 | 0.456 | 0.533 | 0.571 | 0.680 |
| | | MSE | 0.159 | **0.014** | **0.019** | 0.103 | 0.059 | 0.041 | 0.059 | 0.041 | 0.032 | |
| | With Segmentation Improvements | Image 1 | 0.604 | 0.668 | 0.685 | 0.685 | 0.685 | 0.616 | 0.610 | 0.650 | 0.671 | 0.689 |
| | | Image 2 | 0.606 | 0.658 | 0.666 | 0.647 | 0.666 | 0.610 | 0.612 | 0.683 | 0.685 | 0.657 |
| | | Image 3 | 0.606 | 0.658 | 0.692 | 0.612 | 0.692 | 0.617 | 0.605 | 0.688 | 0.677 | 0.645 |
| | | Image 4 | 0.132 | 0.598 | 0.590 | 0.595 | 0.585 | 0.296 | 0.401 | 0.479 | 0.519 | 0.680 |
| | | MSE | 0.140 | **0.021** | 0.026 | **0.023** | 0.027 | 0.099 | 0.073 | 0.053 | 0.042 | |
| Median | Without Segmentation Improvements | Image 1 | 0.621 | 0.688 | 0.738 | 0.738 | 0.635 | 0.627 | 0.669 | 0.689 | 0.690 | 0.689 |
| | | Image 2 | 0.621 | 0.691 | 0.743 | 0.743 | 0.743 | 0.628 | 0.632 | 0.715 | 0.716 | 0.657 |
| | | Image 3 | 0.622 | 0.680 | 0.718 | 0.585 | 0.718 | 0.643 | 0.619 | 0.734 | 0.702 | 0.645 |
| | | Image 4 | 0.041 | 0.694 | 0.709 | 0.707 | 0.712 | 0.281 | 0.511 | 0.580 | 0.611 | 0.680 |
| | | MSE | 0.161 | **0.013** | 0.031 | 0.030 | 0.032 | 0.101 | 0.046 | 0.037 | **0.027** | |
| | With Segmentation Improvements | Image 1 | 0.622 | 0.684 | 0.735 | 0.735 | 0.735 | 0.633 | 0.627 | 0.663 | 0.687 | 0.689 |
| | | Image 2 | 0.637 | 0.679 | 0.739 | 0.741 | 0.739 | 0.642 | 0.643 | 0.709 | 0.710 | 0.657 |
| | | Image 3 | 0.624 | 0.676 | 0.715 | 0.630 | 0.715 | 0.639 | 0.622 | 0.733 | 0.697 | 0.645 |
| | | Image 4 | 0.084 | 0.662 | 0.670 | 0.671 | 0.671 | 0.290 | 0.454 | 0.540 | 0.577 | 0.680 |
| | | MSE | 0.150 | **0.011** | 0.029 | **0.024** | 0.029 | 0.099 | 0.059 | 0.044 | 0.032 | |

Table 6.1: Table with the comparison of the G-Ratio values measured by each algorithm.

| | | Otsu | Luminance Threshold-ing | Entropic Threshold | Renyi's Entropy | Tsallis' Entropy | Gaussian Smooth-ing | BLIST | Euler Number Optimization (crop) | Euler Number Optimization | Manual Measure-ments |
|---|---|---|---|---|---|---|---|---|---|---|---|
| Without Segmentation Improvements | Image 1 | 1343 | 2866 | 2364 | 2364 | 2364 | 1760 | 1490 | 2559 | 2887 | 3907 |
| | Image 2 | 648 | 2058 | 2098 | 1975 | 2098 | 764 | 850 | 2455 | 2493 | 5142 |
| | Image 3 | 1279 | 2696 | 2825 | 631 | 2825 | 1782 | 1232 | 2571 | 2923 | 4234 |
| | Image 4 | 119 | 1755 | 1414 | 1469 | 1280 | 1017 | 2021 | 2161 | 2175 | 2641 |
| | MSE | 1618 | 927 | 973 | 1293 | 984 | 1424 | 1450 | **867** | **790** | |
| With Segmentation Improvements | Image 1 | 5194 | 3733 | 2557 | 2557 | 2557 | 4898 | 5073 | 4102 | 3680 | 3907 |
| | Image 2 | 5508 | 3681 | 2241 | 2108 | 2241 | 5167 | 5027 | 3162 | 3089 | 5142 |
| | Image 3 | 5522 | 4083 | 3218 | 6302 | 3218 | 4986 | 5573 | 2772 | 3649 | 4234 |
| | Image 4 | 5176 | 2360 | 1882 | 1933 | 1685 | 6438 | 4326 | 3632 | 3396 | 2641 |
| | MSE | 786 | **376** | 860 | 994 | 873 | 999 | 613 | 665 | **569** | |

Table 6.2: Table with the comparison of the number of structures detected by each algorithm.

# Chapter 7

# Conclusions and Future Work

The main objective of this project was the creation of a fully automated method for the segmentation and morphometry of sciatic nerve images gathered resorting to light microscopy. To do so, a review on the literature was necessary so that various algorithms could be tested and the best one chosen to integrate the solution. A correct segmentation is essential to this problem, or the measurement of the characteristics will be strongly affected by the segmentation errors.

There are already a few attempts to solve the sciatic nerve segmentation and morphometry problem for electron microscopy, in the literature, but the optical microscopy has been left aside. An extensive research on the literature, regarding algorithms that may apply to this segmentation problem, was done. Due to the size of the images, most adaptive thresholding algorithms tested take hours, sometimes more than a day, to run. Therefore, those algorithms were not considered in this study, hence why most algorithms described and compared in this document are global. The study done and algorithm comparison represent a strong advance for this specific image processing problem.

The segmentation algorithm suggested in this work, albeit simple, may prove useful for various image processing problems with similar characteristics. The results of its application to this specific problem, although not bad, were bested by other algorithms present in the literature, namely the Luminance Thresholding and the Entropic Threshold.

The algorithm suggested by Khashman and Sekeroglu, originally for text enhancement in a document, presented very good results. In the segmentation phase, this algorithm correctly segmented an average of 88.5% of the pixels in the image compared with the ground truth, a manually segmented set of images.

A method for measuring the image characteristics, being the G-Ratio the most important, was also implemented. This technique presented with great results, having only 1% MSE.

Using the Luminance Thresholding for segmentation and the algorithm presented in this work for morphometry, a fully automated process was developed, also with very

interesting results. The final measurements of the G-Ratio had about 2.1% MSE, when compared with the manual process readings done by IBMC researchers. With the segmentation improvements and using the median instead of the mean to calculate the G-Ratio, the error is reduced to 1.6%. Although there is some improvement, the results may be unpredicted for other images, due to the introduction of outliers in the segmentation improvement step and the 0.5% improvement may not be worth the risk. With a proper algorithm for the removal of invalid axons, though, this value could improve even more, and using the median instead of the mean may also be a viable option.

The full process should take about 5 to 7 minutes to run on a Core i5 330M, HDD Sata 5400 rpm and 4GB RAM, depending on the images, with the Matlab® R2010a implementation. Although a low run time was not a primary objective, it is still worth noting.

When considering Khashman and Sekeroglu's method without segmentation improvement, the axon count was about 23% below the manually estimated values. This is mainly due to the object that are considered as merged after the initial segmentation process. The manual count values are statistically inferred since, as previously mentioned, only 250 structures are measured. This method measures an average of 2344 structures per image, which represents a 837.5% increase, although some detected structures are false-positives. To improve the correctness of this measure, the algorithm for removing unwanted structures need to be developed, so that the splitting method can be used. Improvements to the splitting method can also lead to better results, so it should be considered in the future work.

Also, no tool is yet available for the researchers to use for this specific problem, but the results from this work may serve as a starting point for future development.

Globally, the work done successfully completed the proposed objectives. There is, obviously, room for future improvement, as has already been stated.

# References


[BL79] S. Buecher and C. Lantuejoul. Use of watershed in contour detection. In *Proc. Int. Workshop Image Processing, Real-Time Edge and Motion Detection/Estimation, Rennes, France*, pages 17–21, 1979.

[CH09] T. Chomiak and B. Hu. What is the optimal value of the g-ratio for myelinated fibers in the rat cns? a theoretical approach. *PLoS ONE*, 4(11):e7754, 11 2009.

[Col07] T.J. Collins. ImageJ for microscopy. *Biotechniques*, 43(1):25–30, 2007.

[dAEMdA04] M.P. de Albuquerque, I.A. Esquef, A.R.G. Mello, and M.P. de Albuquerque. Image thresholding using tsallis entropy. *Pattern Recognition Letters*, 25(9):1059–1065, 2004.

[dSJF07] A.P.D. da Silva, C.E.R. Jordão, and V.P.S. Fazan. Peripheral nerve morphometry: Comparison between manual and semi-automated methods in the analysis of a small nerve. *Journal of Neuroscience Methods*, 159(1):153 – 157, 2007.

[KS07] A. Khashman and B. Sekeroglu. A novel thresholding method for text separation and document enhancement. In *Proceedings. 11th Panhellenic Conference in Informatics*, pages 324–330, 2007.

[KSW85] J.N. Kapur, P.K. Sahoo, and A.K.C. Wong. A new method for gray-level picture thresholding using the entropy of the histogram. *Computer vision, graphics, and image processing*, 29(3):273–285, 1985.

[LSC07] M.R. Lamprecht, D.M. Sabatini, and A.E. Carpenter. CellProfiler$^{TM}$: free, versatile software for automated biological image analysis. *Biotechniques*, 42(1):71, 2007.

[LTA02] R.J. Lapeer, A.C. Tan, and R. Aldridge. A combined approach to 3d medical image segmentation using marker-based watersheds and active contours: the active watershed method. *Medical Image Understanding-MIUA*, pages 165–168, 2002.

[NAP00] A. Nedzved, S. Ablameyko, and I. Pitas. Morphological segmentation of histology cell images. In *Proceedings in 15th International Conference on Pattern Recognition*, volume 1, pages 500 –503 vol.1, 2000.

[Ots75] N. Otsu. A threshold selection method from gray-level histograms. *Automatica*, 11:285–296, 1975.

[PRGC11] T. Pinto, A. Rebelo, G. Giraldi, and J.S. Cardoso. Music score binarization based on domain knowledge. In *Proceedings of Iberian Conference on Pattern Recognition and Image Analysis (IbPRIA)*, pages 700–708, 2011.

[RCD+00] E. Romero, O. Cuisenaire, J.F. Denef, J. Delbeke, B. Macq, and C. Veraart. Automatic morphometry of nerve histological sections. *Journal of Neuroscience Methods*, 97(2):111 – 122, 2000.

[SWY97] P. Sahoo, C. Wilkins, and J. Yeager. Threshold selection using renyi's entropy. *Pattern recognition*, 30(1):71–84, 1997.

[Tsa95] D.M. Tsai. A fast thresholding selection procedure for multimodal and unimodal histograms. *Pattern Recognition Letters*, 16(6):653–666, 1995.

[VH98] M.W. Vannier and J.W. Haller. Biomedical image segmentation. In *Proceedings of the Internation Conference on Image Processing*, volume 2, pages 20–24, October 1998.

[VM09] J. Vromen and B. McCane. Red blood cell segmentation from sem images. In *Internation Conference on Image and Vision Computing, New Zealand*, pages 44 –49, 2009.

[VS91] L. Vincent and P. Soille. Watersheds in digital spaces: an efficient algorithm based on immersion simulations. *IEEE Transactions on Pattern Analysis and Machine Intelligence*, 13(6):583–598, jun 1991.

[ZPW+10] X. Zhao, Z. Pan, J. Wu, G. Zhou, and Y. Zeng. Automatic identification and morphometry of optic nerve fibers in electron microscopy images. *Computerized Medical Imaging and Graphics*, 34(3):179 – 184, 2010.